Chemical Geology 629 (2023) 121493

Contents lists available at ScienceDirect

Chemical Geology

journal homepage: www.elsevier.com/locate/chemgeo

The role of zircon in hydrothermal heavy REE mineralisation: The case for unconformity-related ore deposits of north-west Australia

Jessica M.J. Walsh *, Carl Spandler

Australian Critical Minerals Research Centre, School of Physics, Chemistry and Earth Sciences, Faculty of Sciences, Engineering and Technology, The University of Adelaide, Adelaide, SA 5005, Australia

ARTICLE INFO

Editor: Balz Kamber

Keywords:
Rare earth elements
Zircon
Hydrothermal
Unconformity-related
Critical minerals

ABSTRACT

Zircon is hailed for its chemical and physical durability, but can undergo extensive chemical and structural modification due to radiation damage via the emission of alpha (α) particles, and subsequent low-temperature hydrothermal alteration. Here, we investigate Archean zircons from arkosic metasediments of the Browns Range Metamorphics (BRM) to evaluate their role in the formation of local unconformity-related heavy rare earth element (REE) ore deposits, within the Browns Range Dome, Western Australia. We determine that the heavy REE inventory of the BRM are primarily hosted in zircon, and that these zircons have a wide range of major element totals (77 to ~100 wt%, including low SiO_2 and ZrO_2 contents), and high and variable 'non-formula' components (U, Th, Y, REE, Nb, P, Al, Ca, Fe, Ti, F and OH^- or H_2O). Concentrations of Y + REE in some cases exceed 8 wt%. Extensive radiation damage (metamictisation) is confirmed by structural features including porous and amorphous domains, cavities, and voids. The lack of regional thermal events over an extended period likely prevented thermal annealing of these radiation-damaged zircons. Uptake of non-formula elements in metamict zircon, most likely during sedimentation in the late Archean, promoted further radiation damage, such that these grains remained highly susceptible to alteration by subsequent hydrothermal fluid circulation. We propose that the unconformity-related REE mineralisation was formed by saline fluids leaching Y + REE (and possibly P) from metamict zircon in the BRM, followed by ore mineral precipitation in fault zones near, and along the regional unconformity. More broadly, this model of ore formation may be relevant to other basin-hosted mineral systems, and could be used to guide exploration for unconformity-related REE deposits in Australia, and globally.

1. Introduction

The transition to a high-tech society powered by renewable energy is driving increasing demand for critical metals such as rare earth elements (REEs), yet ongoing supply of these metals is at risk due to the geopolitics of global trade, and growing requirements for environmentally and socially responsible mining and mineral processing practices (Ali et al., 2017; Bruce et al., 2021). The imperative for diversity of supply of REEs is propelling exploration for new styles of mineralisation across the globe (e.g., Spandler et al., 2020). This is particularly relevant for heavy (H)REEs for which there are currently few alternative sources outside of China.

Unconformity-related REE deposits are a recently defined mineralisation style, based on the ore deposits and prospects of the Browns Range Dome, Western Australia (Nazari-Dehkordi et al., 2018; Fig. 1). Unlike most other REE ore styles, mineralisation is distinctively HREE rich, is definitively of low temperature (i.e., $T < 300$ °C) hydrothermal origin, and is hosted in metasedimentary rocks with no apparent association with alkaline magmatism (Nazari-Dehkordi et al., 2017; Nazari-Dehkordi et al., 2018; Nazari-Dehkordi et al., 2020). The REEs are derived from basement metasedimentary rocks of the Browns Range Metamorphics (BRM; Nazari-Dehkordi et al., 2017), yet how these elements are mobilised and concentrated to form orebodies remains a mystery, especially considering that REE-rich minerals, and particularly HREE-rich minerals, are known to be highly insoluble in low temperature hydrothermal fluids (Migdisov et al., 2016; Williams-Jones, 2015). Resolution to this conundrum is needed to not only understand how hydrothermal REE orebodies form, but also for developing effective mineral exploration strategies to ensure the ongoing discovery of the ore deposits that will be needed to meet global REE demand into the future.

* Corresponding author.
E-mail address: jessica.walsh@adelaide.edu.au (J.M.J. Walsh).

https://doi.org/10.1016/j.chemgeo.2023.121493
Received 16 December 2022; Received in revised form 13 April 2023; Accepted 16 April 2023
Available online 20 April 2023

In this study we aim to progress the understanding of how REEs are mobilised by hydrothermal fluids, via detailed examination of the mineral hosts of REEs in the BRM; the recognised source of the REEs for mineralisation in the region. Our primary focus is on zircon, which is an important HREE host and a robust U—Pb geochronometer widely used to provide information for provenance studies (Yang et al., 2022), igneous petrology (Hoskin and Schaltegger, 2003), metamorphic and impact processes (Rubatto, 2002; Wittmann et al., 2006), and early Earth history (Hoskin, 2005; Valley et al., 2014; Wilde et al., 2001).

However, zircon has an Achilles heel; namely its affinity for U and Th results in radiation damage to the crystal structure (metamictisation) over time, which then allows for uptake of non-formula elements, as well as susceptibility to fluid-aided alteration even under low temperature (i.e., $T < 300$ °C) conditions (Delattre et al., 2007; Geisler et al., 2003a; Geisler et al., 2003b; Hay and Dempster, 2009a; Hay and Dempster, 2009b; Nasdala et al., 2001b; Pidgeon et al., 2019). These processes are particularly relevant for ancient zircons, such as the Archean zircons of the BRM (Nazari-Dehkordi et al., 2017), that have billions of years to undergo metamictisation. By employing a combination of micro- and nano-analytical techniques, we document the unusual composition and structure of the BRM zircons that arguably make them amenable firstly to REE uptake, and then subsequently to REE liberation by fluids. These results provide insights into how hydrothermal REE ore deposits form and may guide strategies for locating and identifying REE deposits in sedimentary basins across the globe.

2. Geological framework

2.1. Unconformity-related REE ore deposits

Heavy REE mineralisation at the Browns Range Dome, located in the northern Tanami region of northern Western Australia (Fig. 1), occurs as numerous orebodies that mostly are hosted along or immediately beneath a regional unconformity surface between late Archean siliciclastic metasedimentary rocks of the BRM and the overlying Mesoproterozoic Gardiner Sandstones of the Birrindudu Group (Nazari-Dehkordi et al., 2017). The orebodies consist predominantly of xenotime [(Y,HREE)PO_4] plus quartz with minor florencite [LREEAl_3(PO_4)$_2$(OH)$_6$], and occur along steeply-dipping structures within a stockwork of hydrothermal veins and breccias (Nazari-Dehkordi and Spandler, 2019). The mineralisation is reported to have formed between 1.65 and 1.60 Ga at a time of tectonic quiescence, and with no links to contemporaneous magmatism or metamorphism (ca. 1.83 to 1.72 Ga local metamorphism; Nazari-Dehkordi et al., 2020). Samples of the BRM are variably depleted in (H)REE compared to the sedimentary protoliths. They also have non-radiogenic Nd isotope compositions that are comparable to the orebodies, but are quite distinct from the igneous rocks or other sedimentary rocks (e.g., Birrindudu Group) of the North Australian Craton (Nazari-Dehkordi et al., 2017). These observations demonstrate that the REEs responsible for ore formation were derived directly from the BRM. Mineralisation is interpreted to have occurred via mixing between saline REE-bearing basinal fluids (with up to 25 wt% salinity and approximate $T = 200$ °C), and acidic P-bearing fluids from the overlying sequences (Nazari-Dehkordi et al., 2019). Focussed fluid flow in fault and breccia zones drove local rock alteration toward a fluid-buffered mineral assemblage of quartz plus muscovite (Nazari-Dehkordi et al., 2018). This mineralisation style is unusual for REE deposits, as it is purely hydrothermal, but has been recognised across north-western Australia (Fig. 1), including from the western Tanami (Watts Rise-Castella also known as Killi Killi Hills) and Halls Creek Orogen (John Galt), as well as the Athabasca Basin, Canada (Maw Zone; Rabiei et al., 2017).

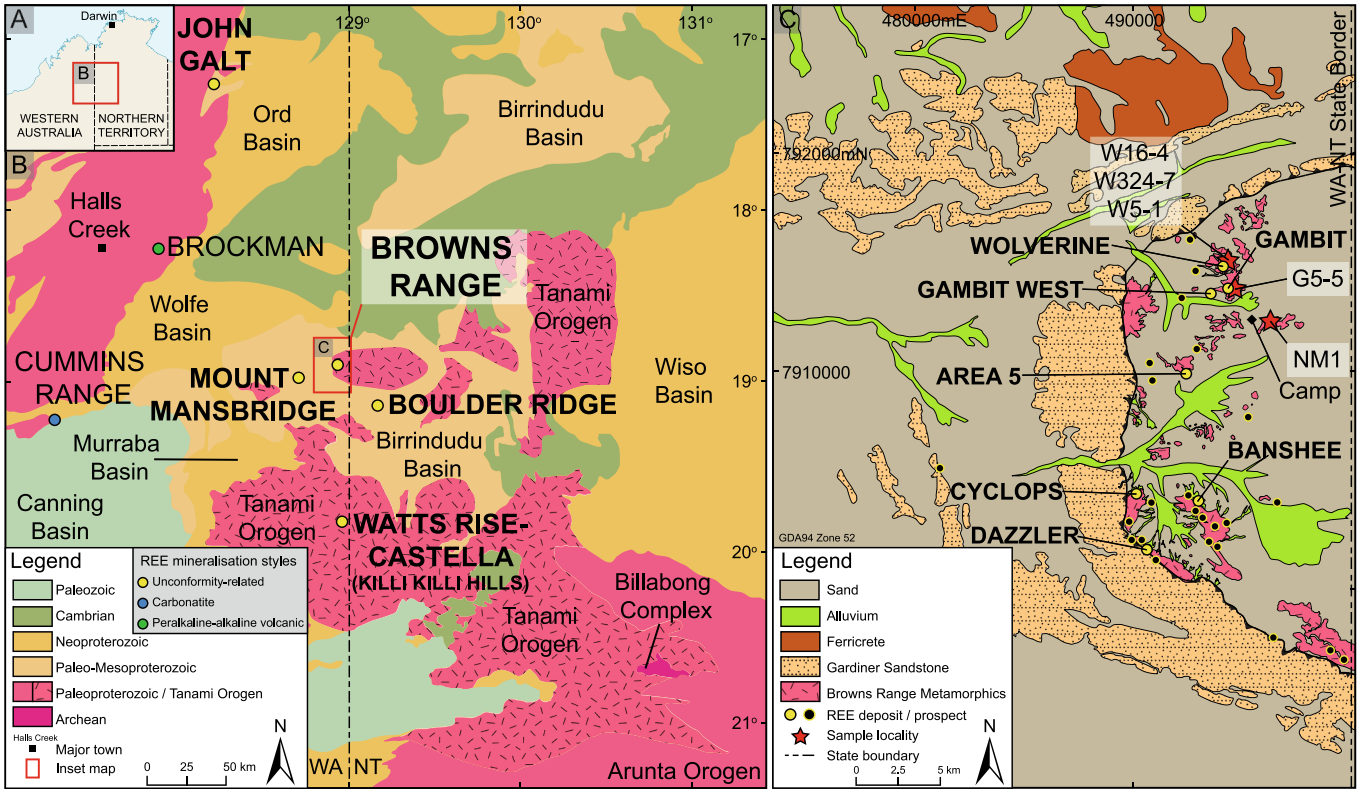

Fig. 1. (a) Location of the field area in relation to northern Australia. (b) Simplified basement geology of the Tanami region of Western Australia (WA) and Northern Territory (NT), with the locations of major hard-rock REE occurrences and mineralisation styles in northern Australia. (c) Geology of the western margin of the Browns Range Dome. Hydrothermal unconformity-related REE deposits and prospects are shown. The non-mineralised Browns Range Metamorphic (BRM) samples examined in this study are indicated by red stars. Adapted from Ahmad et al. (2013), Morin-Ka et al. (2016), Nazari-Dehkordi et al. (2018), and Nazari-Dehkordi and Spandler (2019). (For interpretation of the references to colour in this figure legend, the reader is referred to the web version of this article.)

2.2. Browns range metamorphics

The BRM are a package of immature quartzofeldspathic, meta-arkosic sandstones, with minor medium- to coarse-grained interbedded conglomerates, and less common banded ironstone, semi-pelitic schists, and calc-silicate units (Blake et al., 2000; Nazari-Dehkordi et al., 2017; Nazari-Dehkordi et al., 2018). Altered granitic clasts occur with the conglomeritic units and sporadically within the arkosic units (Nazari-Dehkordi et al., 2017). The BRM outcrop discontinuously over an area of ~100 km^2, on the western and southern margins of the granite-cored Browns Range Dome (Fig. 1). The unit is unconformably overlain by the Paleoproterozoic to Mesoproterozoic Gardiner Sandstone and Dead Bullock Formation of the Birrindudu Group (Blake et al., 2000), and intruded by the Browns Range Dome granite (Nazari-Dehkordi et al., 2017). Rock outcrop is limited, which has inhibited detailed stratigraphic work, including determining the true thickness of the package. However, the estimated thickness is between 1000 and 3000 m (Maidment et al., 2020). The BRM has experienced relatively low-grade greenschist-facies (but locally up to amphibole-facies) regional metamorphism at between ca. 1.83 Ga (Crispe et al., 2007) and 1.72 Ga. This latter age is recorded by Ar—Ar dating of pre-ore muscovite from the BRM (Nazari-Dehkordi et al., 2020). The package has been intruded by numerous granite and pegmatite bodies (2.5 Ga) and mafic-ultramafic rocks that were also affected by regional metamorphism. Analysis of zircons from the BRM by Nazari-Dehkordi et al. (2017) reveal a single detrital population of ca. 3.0 to 3.2 Ga, with the zircons having undergone variable levels of Pb loss. Bulk geochemical compositions are compatible with a granitic source for the sediment, although with very low contents of CaO and P_2O_5 (Nazari-Dehkordi et al., 2017). The BRM are therefore interpreted to represent clastic detritus shedding off a Mesoarchean granitic source over a depositional window of between ca. 3.0 to 2.5 Ga (Nazari-Dehkordi et al., 2017).

2.3. Sample description

Unmineralised BRM samples selected here for detailed mineralogical analysis include NM1, W5–1, W324–7, W16–4, and G5–5, as described by Nazari-Dehkordi et al. (2017). Sample NM1 was collected from a surface outcrop, whereas the other samples were collected from drillcore at ~100 m depth (W16–4 and G5–5) and ~ 441 m depth (W5–1 and W324–7). The samples are typically immature, coarse-grained (>1.5 mm grains), arkosic meta-sandstones exhibiting a weak to strong foliation, and some with minor interbedded finer (< 0.5 mm grains) layers. The BRM samples are all dominated by quartz (~60 to 80%) with lesser amounts of muscovite and orthoclase (3 to 20% each), and accessory minerals (in order of abundance) illite, iron oxides, rutile, and zircon. Zircon accounts for ~0.03% of the samples and is described further below. Notably, the low bulk rock CaO and P_2O_5 contents means that these rocks are devoid, or almost devoid, of accessory calcite, apatite, and/or titanite, which is unusual for clastic quartzo-feldspathic meta-sedimentary rocks.

We also analysed a core sample (W5–11) of intensely-foliated quartz-sericite rock from an approximately 1 m wide shear zone located at 544.5 m depth, below the Wolverine Deposit. The sample consists of bands (2–3 mm) of fine- to medium-grained foliated muscovite (~50 modal %) wrapping partly diassgregated granoblastic bands (grainsize ~0.5 to 2 mm) of deformed quartz (~45 modal %) and minor K-feldspar (~5 modal %). Accessory minerals include rutile (up to 0.5 mm) zircon and florencite. The sample represent a product of fluid-dominated rock alteration (e.g., Nazari-Dehkordi et al., 2018), but is not mineralised, and therefore is studied to inform on ore element migration associated with fluid alteration.

3. Methods

Polished rock blocks, thin sections, and epoxy zircon grain mounts for all samples were imaged and analysed for chemical, mineralogical, spectroscopic, and structural composition at The University of Adelaide, Australia. Below, we present a summary of the analytical procedures used in this study. Full details of all analytical methods are presented in Appendix 1.

3.1. Mineral modes and mineral compositions of BRM samples

Automated mineralogy maps of polished rock blocks of the BRM samples were obtained using a Bruker QUANTAX energy dispersive spectrometry (EDS) system attached to a Hitachi SU3800 scanning electron microscope (SEM). Mineral identification was completed using the Bruker Advanced Mineral Identification and Characterisation System (*AMICS*) software. Automated mineralogy maps were used to determine mineral modes and to locate potential REE-bearing phases (e.g., zircon, xenotime, and florencite) for further investigation. Mineral major and trace element compositions were determined on polished rock blocks and zircon grain mounts using a Cameca SX-Five electron probe microanalyser (EPMA), and laser ablation inductively coupled plasma mass spectrometer (LA-ICP-MS), respectively. Two LA-ICP-MS set-ups were employed: (1) RESOlution-LR 193 nm ArF excimer laser ablation system, coupled to an Agilent 8900× ICP-MS for zircon trace element and U—Pb isotope analysis, and (2) NWR213 (Elemental Scientific Lasers) laser ablation system coupled to an Agilent 7900× ICP-MS for trace element analysis of orthoclase, muscovite, and rutile. Florencite and xenotime compositions were taken from Nazari-Dehkordi and Spandler (2019). Quantification of mineral trace element concentrations employed ^{27}Al and ^{47}Ti as the internal standard for orthoclase and muscovite, and for rutile, respectively. Quantification of the zircon trace element compositions proved more challenging due to varying concentrations of the two major elements (Zr and Si) that could be used for internal standardisation, even within the zones of individual zircon grains (see below). The low and variable totals from the EPMA analyses of the zircon also precluded internal standardisation by summing all elements to 100%. Analysis of the major element data did reveal a relationship between the Zr/Y value and Zr content ($R^2 = 0.64$), which could then be used to calculate an 'internal standard' for the Zr content to apply to each zircon analysis. More details on this procedure are outlined in Appendix 1. The BRM zircon samples were also analysed by LA-ICP-MS for U—Pb geochronology following the procedures outlined in Appendix 1.

3.2. Element distribution budgets

Element distribution budgets for REEs, Y, Th, U, and P in four BRM samples (W5–1, W16–4, W324–7, and G5–5) were determined via a mass balance approach that compares the measured bulk rock element concentration (taken from Nazari-Dehkordi et al., 2017) of each sample with a 'calculated' bulk rock element concentration based on the modal proportions and compositions of the constituent minerals. The 'calculated' bulk rock concentrations of each element are the sum of the elemental contribution from each mineral, which was determined by multiplying the average geochemical composition of each mineral by its respective modal proportion.

3.3. Textural, structural and Raman spectroscopic analysis of zircon

Zircon grains in mounts were imaged via backscattered electron (BSE) images obtained using a FEI Quanta 450 field emission gun scanning electron microscope (SEM). Cathodoluminescence images of the grain mounts examined by Nazari-Dehkordi et al. (2017) were also utilised in this study. Subsequent to imaging, and major and trace element analysis, Raman spectra were acquired on select zircon grains using a HORIBA Scientific (Jobin Yvon) LabRAM HR800 integrated confocal Raman spectrometer. Raman spectra were collected to provide estimates for the degree of crystallinity in the zircon structure (Nasdala

et al., 1995; Nasdala et al., 2001b; Palenik et al., 2003). The system was calibrated for each analytical session and analyses were undertaken on exposed half sections of zircon grains in polished epoxy mounts utilising a 532 nm Quantum Laser (150 mW), with 1800 lines per millimetre (l/mm, or 500 nm) grating. Spectra were collected over a wavenumber range from 100 to 4000 cm^{-1}.

For detailed micro- to nano-scale grain characterisation, zircon samples were prepared as foils for transmission electron microscopy (TEM) analysis using a FEI-Helios nanoLab 600 DualBeam™ focused ion beam (FIB) SEM. Six thinned foils were prepared targeting grain domains with variable or high Y + REE and/or Th, as confirmed from previous EPMA and laser ablation ICP-MS analyses. Milling on the surface of the grains and foil cutting was performed under vacuum by using a high energy Ga^{+} ion beam. Each foil was then attached to a Cu grid and extracted using the in-situ lift out technique, as previously outlined by Ciobanu et al. (2011) and Wirth (2009).

The six foils were subsequently examined using high-angle annular dark field (HAADF) scanning transmission electron microscopy (STEM) imaging and Super-X EDS, in both spot analysis and mapping modes. This was conducted with an ultra-high-resolution, probe-corrected FEI Titan Themis STEM, with an operation voltage of 200 kV. This set-up was able to deliver a spatial resolution for imaging of ~1 nm. The EDS spot analyses and elemental maps focused on Zr, Si, Th, P, Y, and REE.

4. Results

4.1. Element distribution budget

The calculated trace element distribution budgets for the BRM are presented in Fig. 2. Calculations were based on the mineral phases in these samples that are potential hosts of REE, Y, Th, U, and P; these being orthoclase, muscovite, and accessory phases zircon, xenotime, florencite, apatite, monazite, and rutile. Although trace-element budgeting can be difficult due to complex mineralogy and grain-size limitations, the distribution of HREE, along with Th, U, and P in samples from the BRM are well-constrained, with a few exceptions.

The data indicate that the majority of REE, Th, U, and P in the BRM are stored in accessory phases, which is consistent with previous studies on trace element distributions in metasedimentary rocks (e.g., Hammerli et al., 2016; Spandler et al., 2003). On average, the HREE are well-balanced at 80% (where 100% represents a total trace element distribution accounted for by the mineral phases in the bulk rock), although this varies between samples (e.g., W5–1 is balanced at 95%, whereas W16–4 is balanced at 65%; Fig. 2). Aside from sample W5–1 (Fig. 2a), which is the only sample that contains observable but rare xenotime, the HREE are primarily hosted in zircon (e.g., in sample G5–5, the zircon hosts at least 85% of bulk rock HREE content; Fig. 2d).

The mass balance for the LREE is significantly poorer, being between 58% (sample W5–1) and 19% (sample G5–5). The major phases identified as contributing to the LREE budget are florencite (15–35%), zircon (9–18%), and xenotime (10–12%). The remaining unaccounted proportion of LREE is likely attributable to an underestimate of the florencite proportion (due to the fine grain-size), and/or micro-inclusions of monazite in the muscovite (Appendix 1). A similar result was obtained for Th and U, which were balanced only to average values of 16% and 56%, respectively. These elements are hosted in zircon and muscovite, and likely, also fine-grained florencite, monazite and xenotime. Phosphorous is also balanced poorly at between 10 and 38% between samples (Fig. 2). Minerals which contribute to the P budget are florencite (5–21%), muscovite (1–15%), orthoclase (2–8%), and zircon (~1%). The remaining unaccounted proportion of P is likely hosted in rare, small (<10 μm) apatite grains.

4.2. Zircon textures

Zircon grains from the BRM samples are generally euhedral to subhedral, and range from 30 to 250 μm in length, with length to width ratios of 1:1 to 4:1. A minority of the grains have well-defined, oscillatory zonation under cathodoluminescence (CL) imaging, whereas most grains appear dark under CL imaging, but feature abundant fractures and cavities, and 'sponge-like' or pitted textures (Fig. 3). Qualitative EDS analyses reveal that these zircons contain variable contents of so-called 'non-formula' elements, such as Y, P, Th, Ca and Al. Identified mineral inclusions in zircon include xenotime and quartz, but these are relatively rare.

Zircon grains in the quartz-sericite shear zone sample W5–11 range in size from ~10 to 200 μm, and have subhedral to anhedral forms. Most

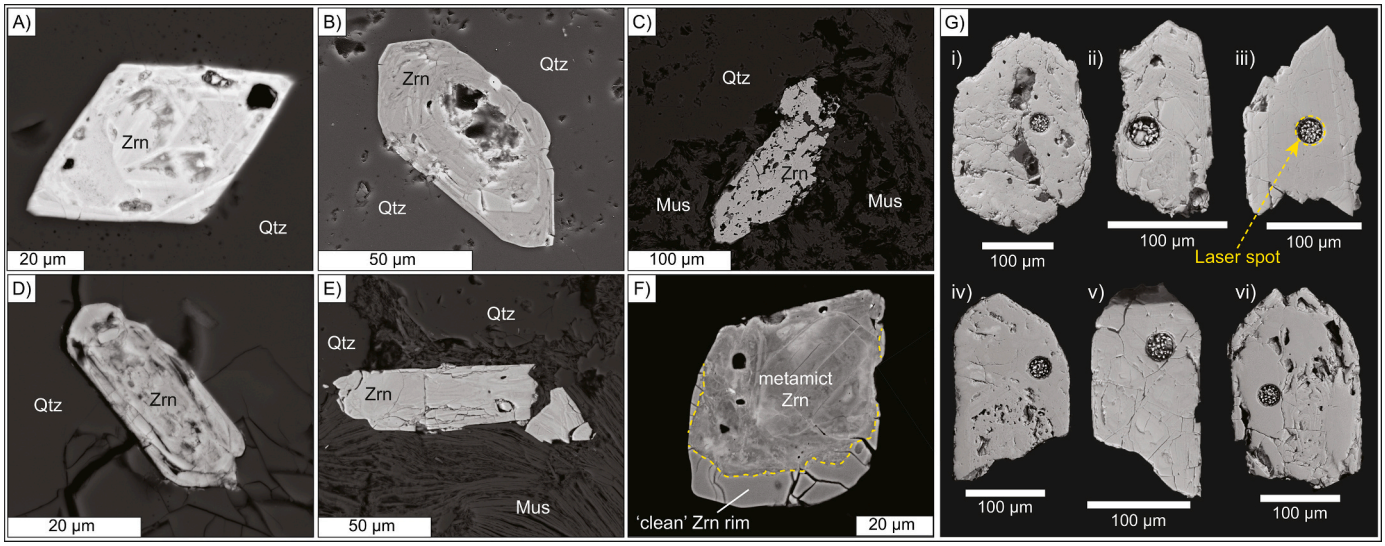

Fig. 2. Element distribution budgets among possible REE-bearing mineral phases (zircon, xenotime, florencite, orthoclase, muscovite, and rutile) of non-mineralised BRM. The 100% dashed line represents the bulk rock composition. Element budgets that do not approach the total of 100% are attributed to unidentified mineral phases (i.e., those with low abundance and small grain size). Graphs (a) to (d) illustrate samples W5–1, W16–4, W324–7, and G5–5, whereas (e) depicts the average of these samples, with the average modal proportions of minerals in the BRM samples shown on the right. Accessory minerals account for <1% of the total mineral assemblage, but host significant amounts of REE, Th, U, and P. The HREE budget of the BRM are dominantly hosted in zircon, which accounts for only 0.03% of the bulk rock mineral assemblage.

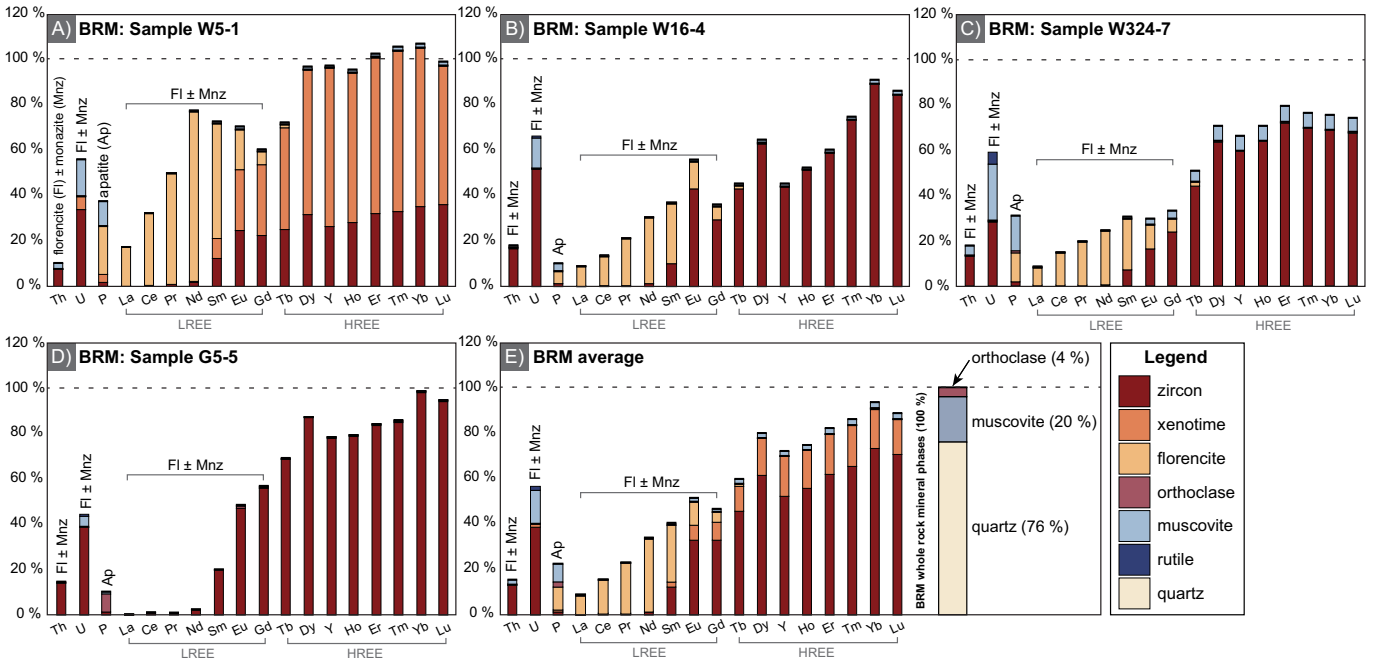

Fig. 3. Backscattered electron (BSE) images demonstrating the morphology and structure of zircon from the BRM. (a) Euhedral zircon with patchy internal zonation and cavities (sample W5–1). (b) Oscillatory zoned and fractured zircon (sample NM-1). (c) Pitted zircon grain with fractures/cavities partly filled by quartz and partly void (sample W5–1). (d) Quartz encasing fractured zircon (sample NM-1). (e) Fractured zircon encased in muscovite (sample NM-1). (f) high-contrast image of shear-zone hosted zircon (sample W5–11) with non-formula element rich metamict core partly rimmed by 'clean' recrystallised zircon. (g) Examples of separated zircon including pervasive cavities and fractures. Where, i) sample W324–7; ii) Sample G5–5; iii) Sample NM1; iv) Sample W16–4; v) Sample W5–1; and vi) Sample W16–4. Abbreviations: Zrn = zircon, Qtz = quartz, Mus = muscovite.

grains have highly chaotic internal zoning texture (as revealed by BSE imaging; Fig. 3F), with levels of P, Y, Th, Al, Ca, and Fe detectable by EDS. These grains often have discontinuous rim zones with homogenous BSE response (Fig. 3F) and low to undetectable (by EDS) levels of non-formula elements.

4.3. Zircon chemistry

4.3.1. Major elements in zircon

Between 24 and 48 EPMA spot analyses of zircon were conducted for each BRM sample (NM1, W5–1, W324–7, W16–4, and G5–5) resulting in 175 analytical spots in total. Detailed results for each analytical point for the samples are provided in Appendix 2.

The BRM zircon analyses yielded a wide range of major element totals (77–102 wt%) with two groups evident; a minority of analyses with totals between 98 and 102%, and the majority with totals of 96% or lower (Fig. 4). Zircons with totals close to 100% have ZrO_2 and SiO_2 contents that are comparable to end-member zircon; however, across the entire dataset, both ZrO_2 and SiO_2 contents decrease linearly with decreasing analytical totals (Fig. 4). The HfO_2 contents are mostly between 1.0 and 1.8 wt%, without correlation to ZrO_2. The zircons also have high and variable concentrations of so-called 'non formula' elements including UO_2 (up to 0.9 wt%), ThO_2 (up to 14.8 wt%), Y_2O_3 (up to 8.5 wt%), P_2O_5, (up to 7.9 wt%), Al_2O_3 (up to 2.4 wt%), CaO (up to 1.6 wt%), FeO (up to 2.7 wt%), TiO_2 (up to 0.5 wt%), and F (up to 0.6 wt %). There is a strong negative correlation between the concentrations of most of these elements and ZrO_2 and SiO_2 (Fig. 5). Although trends with Al_2O_3 and FeO are not well defined, analyses with low totals (and low ZrO_2 and SiO_2) clearly have elevated Al_2O_3 and FeO. Other non-formula elements (MgO, K_2O, Na_2O, Nb_2O_5) tend to have concentrations below 0.2 wt%. Broadly speaking, zircons from the various samples show similar trends, although NM1 zircons tend to have high FeO, Al_2O_3, P_2O_5, and lower CaO and Y_2O_3 compared to the other samples.

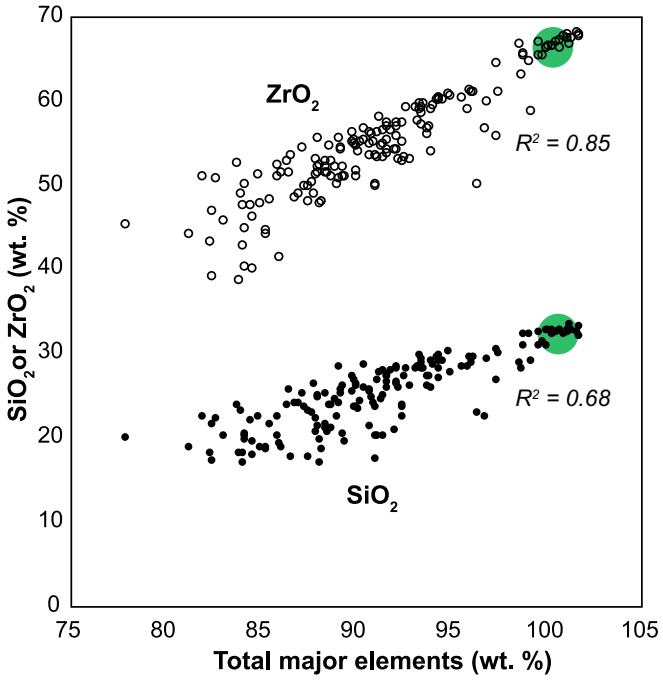

Fig. 4. Binary plot of total major elements (wt%) versus SiO_2 (filled black ellipses, base) and ZrO_2 (empty black ellipses, top) for the BRM zircon. Theoretical endmember pure zircon indicated by the green field (where total major elements = 100 wt%, SiO_2 = 32.5 wt%, and ZrO_2 = 66.5 wt%). Data obtained by EPMA. (For interpretation of the references to colour in this figure legend, the reader is referred to the web version of this article.)

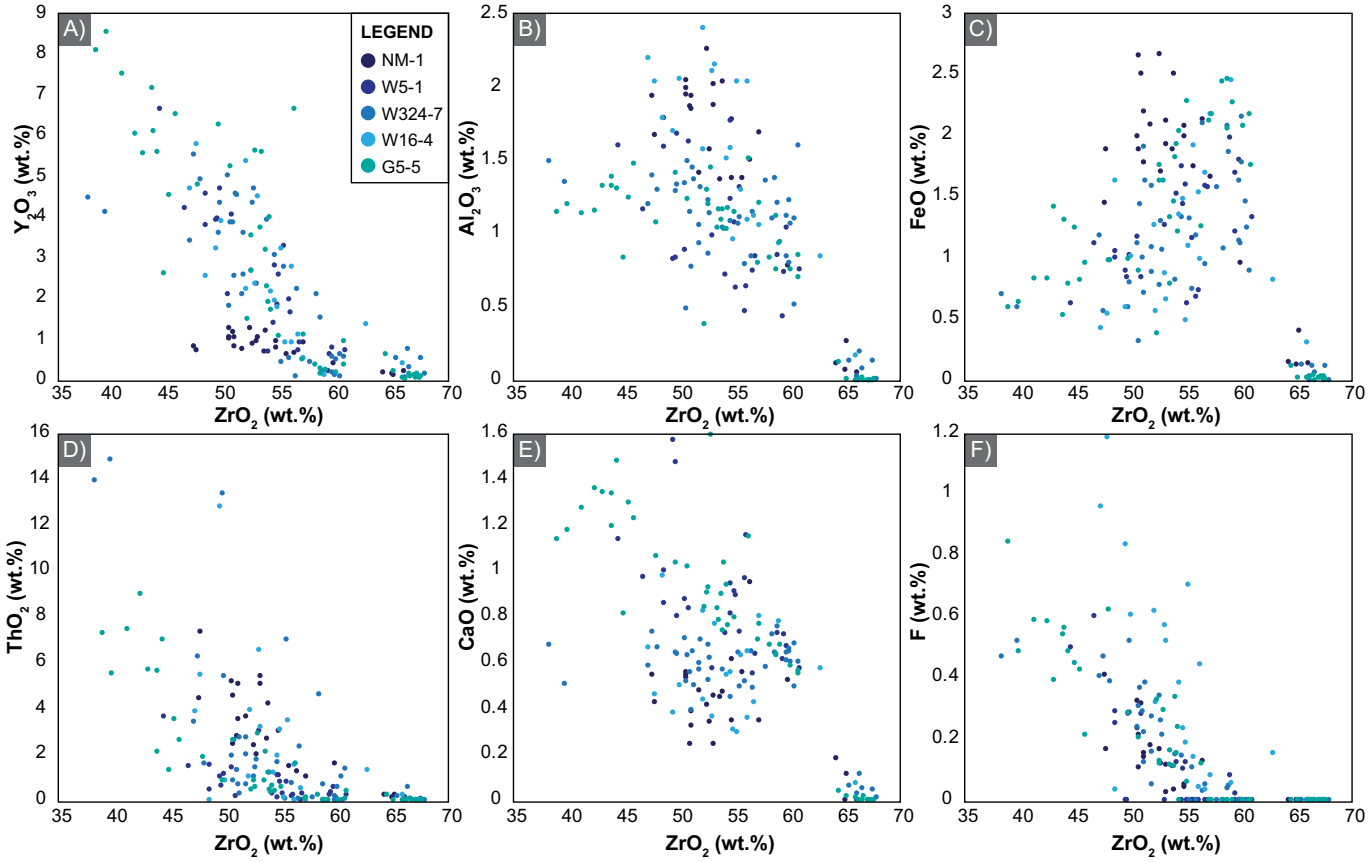

Fig. 5. Scatterplots of selected major element oxides (Y_2O_3, Al_2O_3, FeO, ThO_2, CaO, and F; wt%) against ZrO_2 (wt%) for the BRM zircon. Data obtained by EPMA.

4.3.2. *Trace elements in zircon*

Trace element compositions of 390 zircon grains from all BRM samples were analysed to complement the major element data, although we note that differences in the spatial resolution of data acquisition, and destructive (LA-ICP-MS) vs. non-destructive (EPMA) sampling means the two datasets may not be directly comparable. The trace element compositions for each analytical point are provided in Appendix 2.

Similar to that seen for the major element compositions, the BRM zircons have high and variable contents over a range of trace elements including REE, Y, Nb, Ti, Th, U, and P. Average U and Th concentrations are between 864 and 3727 ppm and 7850 to 32,543 ppm, respectively, which is consistent with the EPMA results. Thorium/U varies significantly from <0.1 to >40, with most being above 3; values that are well above typical magmatic zircon values (Kirkland et al., 2015). Across our dataset we do not observe any clear relationships between Th/U and the concentrations of other elements. By contrast, there are clear positive correlations in the concentrations of most other trace elements, as exemplified by plots of P versus Y, Ti, and Nd, and Nb versus Y (Fig. 6). Again, sample NM1 is distinct, forming correlation arrays between P and Y (Fig. 6a), and Nb and Y (Fig. 6d), that are different from the other samples.

Combined Y and total REE (Y + REE) contents from the zircons are, for the most part, anomalously high, in some cases exceeding 8 wt%. Chondrite-normalised Y + REE patterns for zircon are displayed in Fig. 7 (Palme and O'Neill, 2014), and almost all feature the characteristic positive Ce and negative Eu anomalies that are typical of igneous zircon, with average Ce/Ce* and Eu/Eu* values (Anenburg and Williams, 2022) across all samples being 3.56 and 0.70, respectively (see Appendix 2 for details on individual sample values). The relatively HREE enriched patterns remain consistent, with La_N/Yb_N values across all samples ranging between <0.00 to 0.23 (average 0.01), despite variations in the total Y + REE within and between samples (Fig. 7). Sample NM1 is again the exception having a much larger range of Y + REE pattern slopes and contents, particularly for the light to middle REEs (Fig. 7a). For example, sample NM1 ∑LREE (La to Gd) ranges from 14 to ~18,000 ppm (average 4500 ppm), while in all other samples ∑LREE range ~ 4300 to ~18,500 ppm (average 6600 ppm). Nonetheless, all zircons have significantly higher REE contents than their corresponding bulk rock REE content, and plot similarly to bulk ore (>1.0% total rare earth oxide; TREO; Fig. 7f).

4.4. *Raman*

Crystalline zircon typically exhibits distinct sharp peaks in Raman spectra at 357 cm^{-1}, 439 cm^{-1}, 975 cm^{-1}, and 1008 cm^{-1} (Fig. 8). These peaks correspond to intense vibrational bands involving the SiO_4 tetrahedra and Zr^{4+} cation, and internal SiO_4 symmetric and asymmetric stretching vibration bands (Dawson et al., 1971; Kolesov et al., 2001; Syme et al., 1977). Here, we measured the Raman spectra for BRM zircon grains from 100 cm^{-1} up to 4000 cm^{-1}, to examine a full range of possible spectral features, including the presence of H_2O and/or hydroxl ions in zircon. We also measured spectra for Mud Tank zircon (Gain et al., 2019) using the same analytical conditions in order to provide a reference frame relative for pristine zircon. Baseline corrections were applied to each analysis. Analysis of the Mud Tank zircon produced spectra with sharp, high intensity (e.g., >10,000 a.u. for the main $\nu_3(SiO_4)$ peak at 1008 cm^{-1}) peaks entirely consistent with spectra from crystalline zircon.

Spectra obtained for the BRM zircon were highly variable both between grains and between domains within grains. All of the BRM zircon spectra were strongly attenuated compared to the Mud Tank zircon, with the intensity of the main zircon peak shifted to ~1000 cm^{-1} and only reaching one tenth, or less, of the intensity of the equivalent peak for Mud Tank (Fig. 8). In all cases, BRM zircon peak shapes were

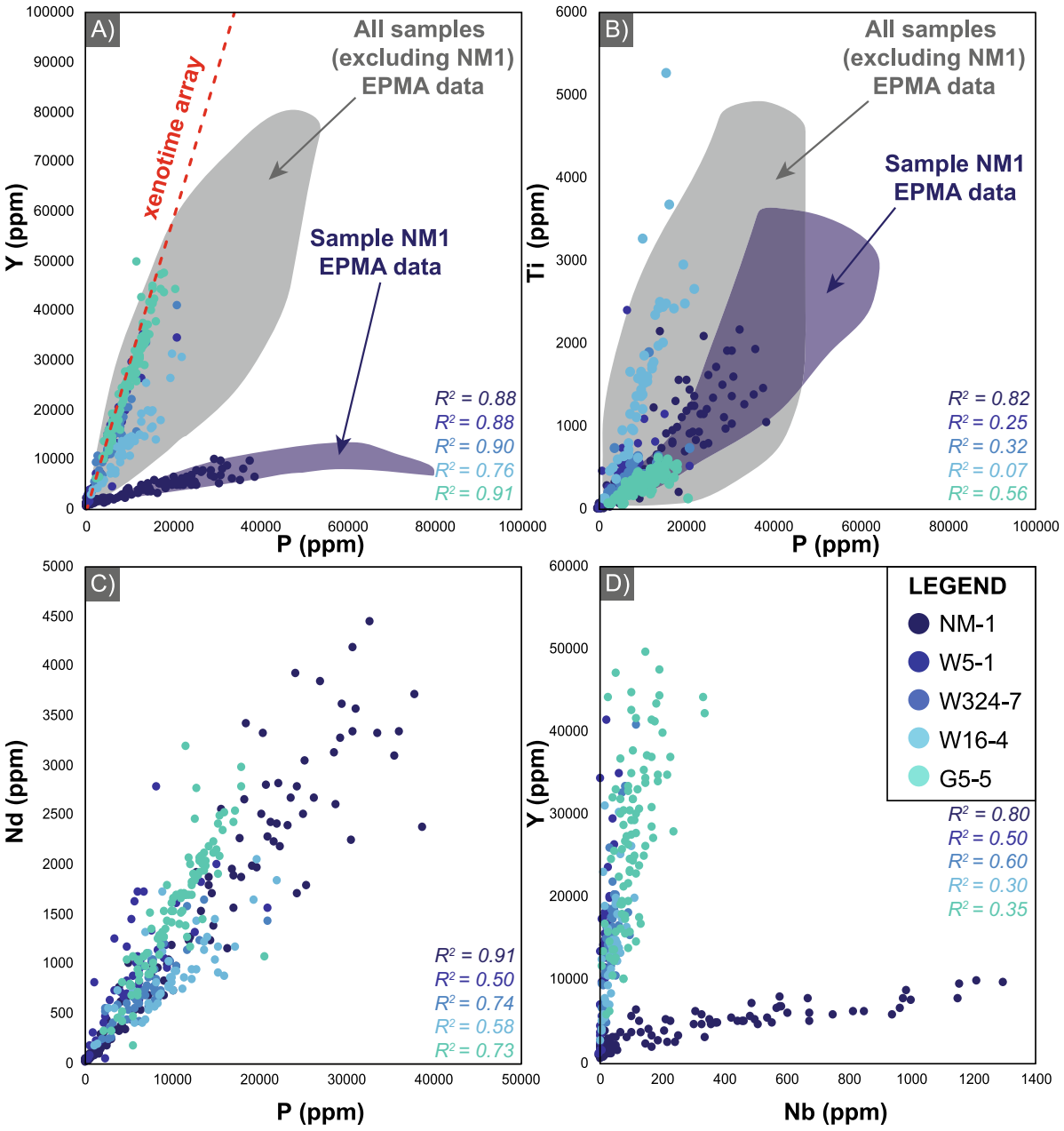

Fig. 6. Scatterplots of selected trace elements (in ppm) for the BRM. All plotted data were acquired by LA-ICP-MS except where stated. (a) Phosphorous versus Y, with the xenotime (assuming YPO_4) substitution array in red. (b) Phosphorus versus Ti. (c) Phosphorus versus Nd. (d) Niobium versus Y. The purple fields (sample NM1) represent data obtained by EPMA. Sample NM1 is distinct from other samples in terms of the Nb-P-Y composition. Note the close correspondence of the LA-ICP-MS and EPMA data. (For interpretation of the references to colour in this figure legend, the reader is referred to the web version of this article.)

significantly broader than for pristine zircon. The BRM zircon spectra also feature a broad convoluted peak of varying intensity between 3100 and 3800 cm^{-1} (Fig. 8b), with a prominent peak at 3400 cm^{-1}; these features are consistent with H_2O, as either hydroxl groups or molecular H_2O, within the crystal structure (Kolesov, 2006; McMillan, 1989; Thomas et al., 2009).

There is a general inverse correlation between the intensity of the 'H_2O' peak region (3100 to 3800 cm^{-1}) and the intensity of the main $\nu_3(SiO_4)$ peak at ~1000 cm^{-1} (Fig. 8), with the BRM zircon domains having the lowest major element totals and the highest content of 'non-formula' elements, along with higher H_2O peaks and lower $\nu_3(SiO_4)$ peaks. In some analyses of zircon with very low major element totals, the $\nu_3(SiO_4)$ peak is not resolvable at all from the spectra. Raman spectra from these zircons commonly feature additional peaks not assigned to zircon, including at 1145 cm^{-1} (Fig. 8a), and a broad composite feature with a peak at 2480 cm^{-1}. These peaks may be due to P—O or U—O stretching (Lv et al., 2016; Ma et al., 2007; Shibata et al., 1981), and P—H or Al-H_2O vibrational bands (Ma et al., 2007; Sergeeva et al., 2019), respectively.

4.5. Nanostructural and chemical characterisation with STEM

Our STEM analysis of six zircon foils from three BRM samples includes high resolution nano-scale (nm-scale) elemental mapping and zircon structural characterisation. In general, we observe similar chemical and structural features in all of the examined samples. Elemental mapping using STEM (nm-scale; Fig. 9) and the highest resolution EPMA maps (step size 1 μm; see Appendix 1) confirm the high REE, Y, Th and P content in zircon, and show that these elements are distributed within distinct oscillatory growth zones (μm to 10s of μm

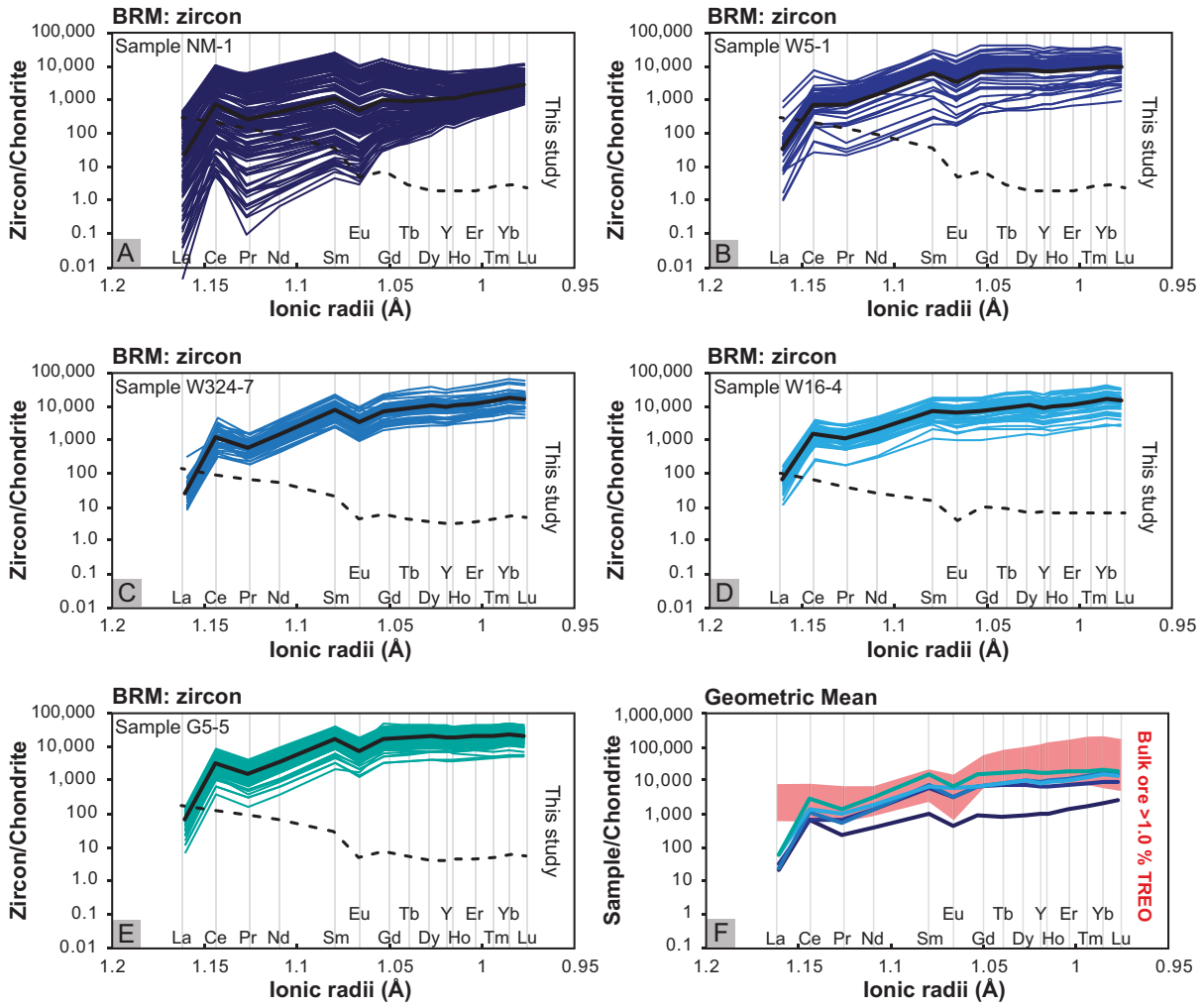

Fig. 7. Chondrite-normalised (Palme and O'Neill, 2014) REE patterns for BRM zircon (a-e), with geometric mean shown in solid black lines and equivalent bulk rock data (Nazari-Dehkordi et al., 2017) in dashed black lines for each sample. (f) Geometric mean of BRM zircon samples, compared to bulk HREE ore samples (>1.0% total rare earth oxide; TREO) from the Browns Range (red field; Nazari-Dehkordi et al., 2017). (For interpretation of the references to colour in this figure legend, the reader is referred to the web version of this article.)

wide; Fig. 9g–k). We also observe elemental enrichments along rare nm-scale linear features that appear to cross-cut the oscillatory zoning (Fig. 9), which we interpret to be nm-scale annealed fractures or fluid alteration zones within the grains. We find no evidence for μm- or nm-scale mineral inclusions that could account for the high content of non-formula elements as determined from EPMA and LA-ICP-MS analysis.

High resolution imaging, including HAADF STEM imaging, of the zircon foils reveal the presence of voids spaces, fractures, and highly porous 'sponge-like' domains (Fig. 9a–g, Fig. 10e–f). These features are observed at both the μm- down to the nm-scale. They were not formed during foil preparation (see Wirth, 2009), and do not have any direct relationship with the distribution of non-formula elements in the zircons. Structural characterisation of trace-element rich zones reveals that the crystallinity of the grains is also not uniform. Lattice misorientation or screw dislocation defects are common (Fig. 10a–b), and semi-crystalline and amorphous zones are present throughout the mineral grains (Fig. 10c–d).

5. Discussion

5.1. Importance of zircon for hosting HREE in metasedimentary rocks

Accessory minerals are commonly the most important hosts of trace elements in metasedimentary rocks (Hammerli and Kemp, 2021; Hammerli et al., 2016; Hermann, 2002; Spandler et al., 2003; Spandler and Pirard, 2013). Our data indicate that zircon is the major repository (60 to 90%) of HREE in the BRM (Fig. 2). This is consistent with the chondrite-normalised REE patterns demonstrating that all BRM zircons have significantly higher REE contents than their corresponding bulk rocks (Fig. 7). This dominance of zircon for hosting the HREE contrasts with other studies of low- to medium-temperature (~350 to 500 °C) garnet-free, clastic metasedimentary rocks, where the HREE are distributed among a number of accessory phases including xenotime, zircon, titanite, apatite, and calcite, with zircon only hosting ~7 to 30% of the HREE (e.g., Hammerli and Kemp, 2021). At higher metamorphic grades, garnet is the dominant HREE host (e.g., Spandler et al., 2003).

An explanation for why zircon dominates the HREE inventory in the BRM is that these rocks have very low bulk CaO contents (average 0.03 wt%) and P_2O_5 contents (average 0.05 wt%; Nazari-Dehkordi et al., 2017), meaning they contain only rare accessory calcite, apatite, and/or titanite (with very little xenotime), which is unusual for clastic quartz-ofeldspathic metasedimentary rocks. There are two possibilities regarding the lack of these REE-hosting mineral phases (i.e., calcite, apatite, and titanite) in the BRM. (i) The BRM represents immature clastic detritus shedding off a Mesoarchean granitic source with an A-type affinity (Nazari-Dehkordi et al., 2017). A-type granites tend to have low bulk CaO and P_2O_5 contents (compared to I- and S-type granites),

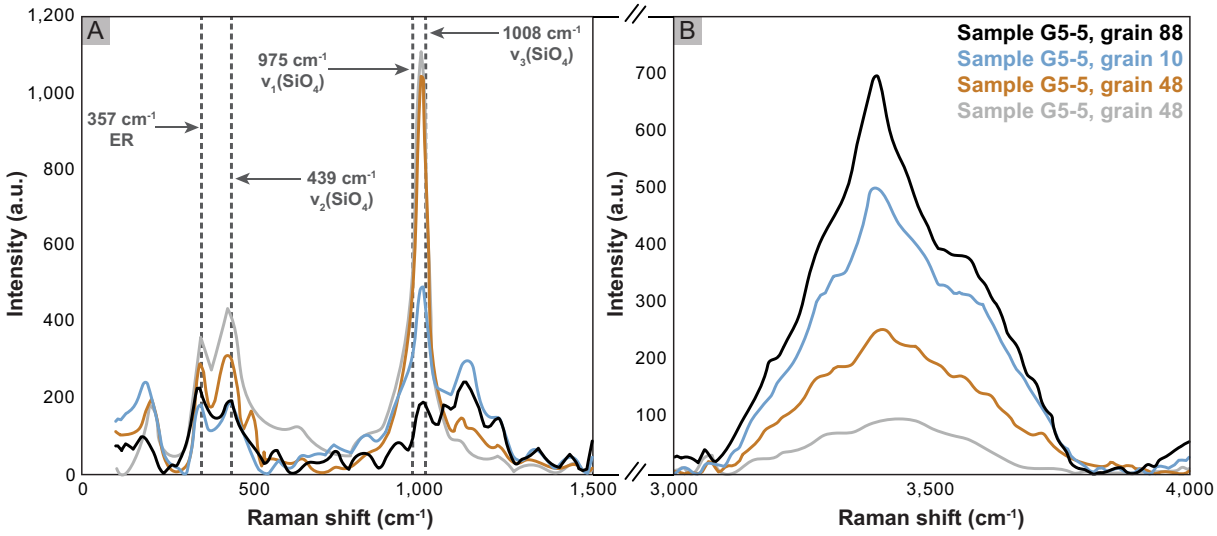

Fig. 8. Representative Raman spectra for the BRM zircon. (a) Raman spectra between 100 cm^{-1} and 1500 cm^{-1} for zircon domains in three grains from sample G5–5. The main vibrational band positions for crystalline zircon are grey dashed lines (Kolesov et al., 2001; Syme et al., 1977). (b) Raman spectra for zircon grains between 3000 cm^{-1} and 4000 cm^{-1}. Note the inverse correlation between the intensity of the main $\nu_3(SiO_4)$ band and the intensity of the main H_2O peak from 3100 to 3800 cm^{-1}. Abbreviations: a.u. = arbitrary units and ER = external rotation Raman band.

and consequently they lack significant amounts of apatite and titanite (Broska et al., 2004; Collins et al., 1982; Whalen et al., 1987). However, we do observe rare apatite grains included in detrital quartz from the BRM (Appendix 1), indicating the host granite did contain at least some apatite. (ii) The BRM, or the source of the BRM, contained other HREE phases such as apatite and titanite, but these were removed or destroyed during erosion and sediment deposition (Harlavan and Erel, 2002), or subsequently during hydrothermal alteration and/or metamorphism. In this case, CaO and P_2O_5 were lost from the rocks, and the released HREE (plus some Th and U) would have been sequestered into the zircon. Further analysis of this latter point is presented below.

Neodymium isotope and REE geochemistry demonstrate that the BRM is the source of REEs for unconformity-related HREE deposits in the region (Nazari-Dehkordi et al., 2018), which in turn implies that these HREE were sourced from zircon in the BRM. With this in mind, we now examine the chemistry and structure of the BRM zircons, with the objective of understanding HREE mobilisation and mineralisation processes.

5.2. Composition of the BRM zircon

Although zircon has been hailed for its chemical and physical durability and robustness, it can undergo significant structural and chemical modification due to: (i) radiation damage due to the emission of alpha (α) particles and subsequent recoil (Cherniak and Watson, 2003; Ewing et al., 2003; Meldrum et al., 1998; Murakami et al., 1991); (ii) intragrain microstructures (e.g., dislocations, low-angle orientation boundaries, and sub grains) formed by crystal-plastic deformation (Reddy et al., 2006); and (iii) hydrothermal, dissolution-reprecipitation reactions (Geisler et al., 2002; Geisler et al., 2007; Hay and Dempster, 2009a).

The BRM zircons are clearly far from pristine ideal zircon in chemistry and crystal structure. Major element analyses yielded a wide range of totals (77–102 wt%) with both ZrO_2 and SiO_2 contents decreasing linearly with decreasing analytical totals (Fig. 4). These zircons also have high and variable concentrations of so-called 'non-formula' elements (including U, Th, Y, REE, Nb, P, Al, Ca, Fe, Ti, and F), and either OH^- or H_2O (Fig. 8) that in general have a strong negative correlation with the ZrO_2 and SiO_2 contents (Fig. 5). Contents of Y + REE, and Th in the zircons can exceed 8 wt%, and 10 wt%, respectively, which is clearly well above the most enriched of igneous zircons (~1 wt% and < 3 wt% respectively; Hoskin and Schaltegger, 2003; Kirkland et al., 2015). There are clear positive correlations between the concentrations of most other trace elements (Fig. 6), despite the elemental systematics of sample NM1 being distinct from the other samples. Micrometre- to nm-scale elemental mapping (Fig. 9) confirm that the high contents of REE, Th, P, and Y in zircon are not due to μm-scale mineral inclusions, but instead indicate element incorporation into the mineral structure, either along oscillatory growth zones or in nm-scale linear features that appear to cross-cut the oscillatory zoning (Fig. 9). These latter features are interpreted to be nm-scale annealed fractures or fluid alteration zones within the grains.

To a large extent, Y + REE, P, and Nb of the BRM zircon can be accounted for by a xenotime substitution mechanism, where $(Y + REE)^{3+} + P^{5+} = Zr^{4+} + Si^{4+}$, or via a $(Y + REE)^{3+} + Nb^{5+} = Zr^{4+} + Si^{4+}$ type substitution (Finch et al., 2001; Hanchar et al., 2001; Finch and Hanchar, 2003; Fig. 6). Sample NM1 is the exception having much higher P and Nb contents compared to Y + REE. Other trivalent elements such as Al^{3+}, and possibly Fe^{3+}, may substitute via similar mechanisms (particularly for NM1), or via substitutions involving $M^{3+} + H^+$ replacing Zr^{4+} (Nasdala et al., 2001a), which would be consistent with the low major element totals and the presence of H_2O as revealed by Raman analysis (Fig. 8b). Any further detailed evaluation of elemental substitution mechanisms may not be particularly meaningful, as our Raman spectra and HAADF STEM imaging reveal extensive amorphization of the zircon structure. Elemental uptake in these amorphous zones can proceed without adherence to crystal lattice constraints of ionic charge balance and ionic radius controls on element substitutions.

The high and variable levels of non-formula elements, and variably low SiO_2 and ZrO_2 contents of the BRM zircons are entirely inconsistent with a primary igneous origin (Hoskin and Schaltegger, 2003). Instead, these characteristics are distinctive of metamict or radiation damaged zircons (Delattre et al., 2007; Geisler et al., 2003b; Hay and Dempster, 2009b), whereby non-formula elements are taken up into radiation-damaged or amorphous domains of the zircon once the inherent radiation dose exceeds the percolation threshhold of 2×10^{18} α-decays/g (Ewing et al., 2003; Fig. 11). Extensive radiation damage to the BRM zircons is confirmed by: (i) structural and textural features of the BRM zircons, including the presence of void spaces, fractures and highly porous 'sponge-like' domains throughout the zircon grains from the μm-down to the nm-scale (Fig. 3, Fig. 9a–g, Fig. 10e–f) and the semi-crystalline to amorphous nature of the grain structure at the nm-scale

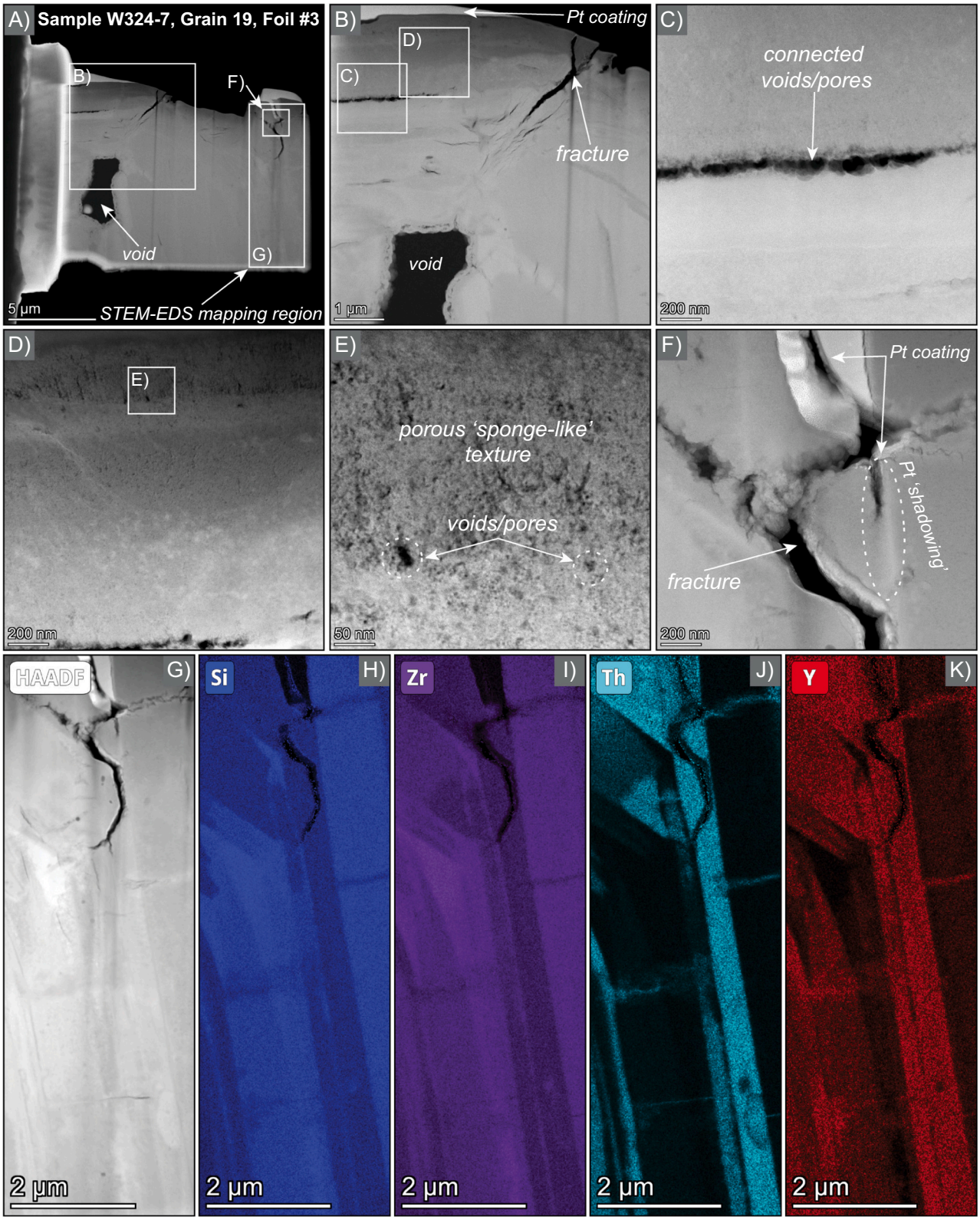

Fig. 9. Summary of STEM and STEM-EDS imaging of a BRM zircon, (sample W324–7, grain 19, foil #3), highlighting structural, textural, and chemical features. (a, b) Overview of sample foil with corresponding areas of interest. (c) Open fracture or linear void structure. (d–e) High-resolution images showing high-porosity zones with 'sponge-like' textures. (f) Fractured domain with nm-scale mineral overgrowth on open fractures (note, the Pt coating in the fracture toward the top of the image is an artefact of foil preparation). (g–k) STEM-EDS maps corresponding to the area indicted in (a). Note the oscillatory growth zonation and inverse concentration relationship between Si + Zr (dark blue and purple) and Th + Y (cyan and red). (For interpretation of the references to colour in this figure legend, the reader is referred to the web version of this article.)

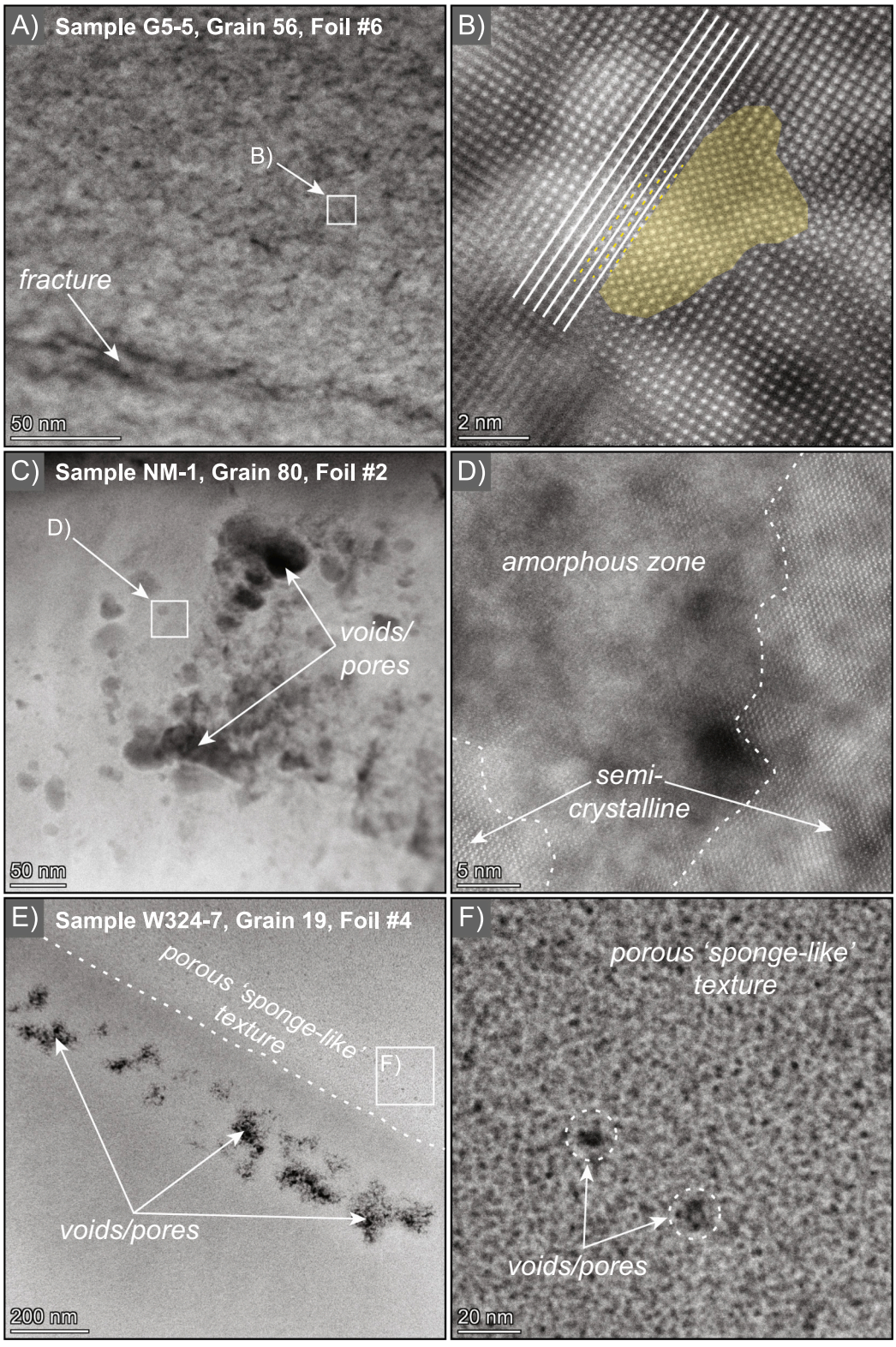

Fig. 10. High resolution HAADF-STEM images of various BRM zircons highlighting nm-scale structural and textural features. (a) Example area from sample G5–5, grain 56, foil #6. (b) High magnification image of the lattice structure demonstrating lattice misorientation or screw dislocation defects with apparent atom replication shown in the yellow field and yellow dashed lines. (c) Example area from sample NM-1, grain 80, foil #2. (d) High magnification image with apparent amorphous zones contrasted against semi-crystalline zircon. (e) Example area from sample W324–7, grain 19, foil #4. (f) High magnification image showing a high-porosity zone with 'sponge-like' texture and numerous void or pore spaces. (For interpretation of the references to colour in this figure legend, the reader is referred to the web version of this article.)

(Fig. 10 b, d); and (ii) complex and variable Raman spectra that include a vibrational band for OH^- and other non-formula components, as well as $\nu_3(SiO_4)$ vibrational bands that are broad and attenuated, or absent altogether (Fig. 8). These have all been documented as features characteristic of high levels of metamictisation of zircon (Chakoumakos et al., 1987; Ewing et al., 2003; Meldrum et al., 1998; Mezger and Krogstad, 1997; Nasdala et al., 1995; Nasdala et al., 2001b; Trocellier and Delmas, 2001; Pidgeon et al., 2019), and are consistent with the high stage II to stage III radiation damage accumulation of Murakami et al. (1991).

Uptake of non-formula elements in metamict zircon is proposed to occcur either by a dissolution-reprecipitation mechanism, which would be facilited by the porous nature of the zircon, or via a diffusion-reaction process (Geisler et al., 2007), or potentially both mechanisms.

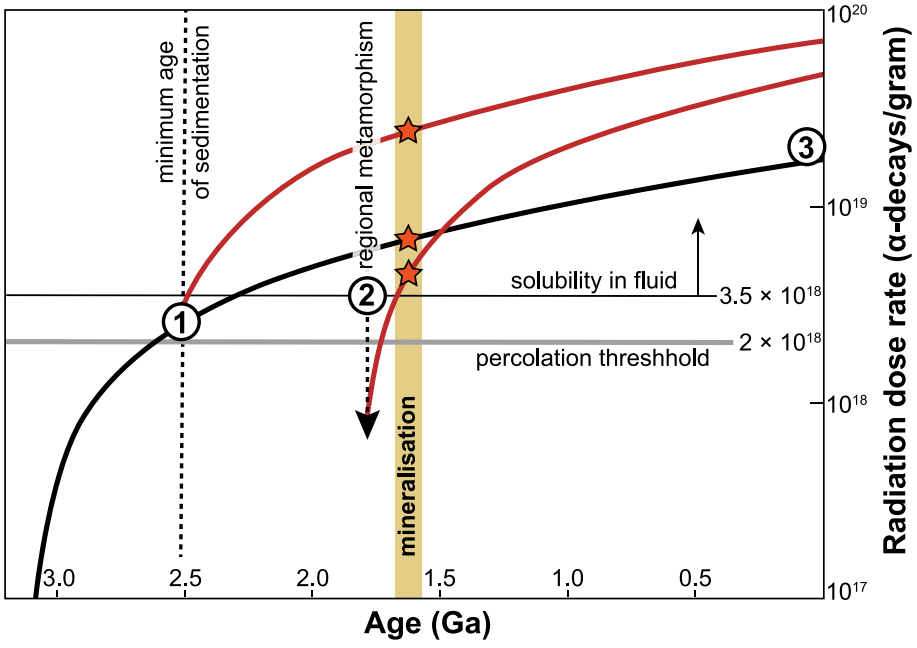

Fig. 11. Age (Ga) versus radiation dose rate (α-decays/g) for the BRM zircons. Radiation dose curves were calculated from the equations of Holland and Gottfried (1955), assuming 1000 ppm each of Th and U in the pristine zircon formed at ca. 3.1 Ga (black curve), and 2500 ppm U and 20,000 ppm Th, for the non-formula enriched metamict zircon (red curves). Uptake of non-formula elements is modelled at ca. 2.6 Ga (sedimentation), ca. 1.8 Ga (metamorphism), and at present day (modern day weathering). See text for details. We consider a component of thermal annealing of the zircons during the ca. 1.8 Ga metamorphism, which is modelled as an 'apparent' decrease in radiation dose at this time. The 1st percolation threshold (from Nasdala et al., 2004) is where aperiodic domains in the zircon structure become interconnected, and the threshold for solubility increase is taken from Ewing et al. (2003). The mineralisation age is taken from Nazari-Dehkordi et al. (2020). As represented by the orange stars, the zircons in all three scenarios would be highly amenable to fluid leaching at the timing of mineralisation (1.65 to 1.60 Ga; Nazari-Dehkordi et al., 2020). (For interpretation of the references to colour in this figure legend, the reader is referred to the web version of this article.)

Regardless, it is clear that this elemental uptake will obscure the primary chemical composition of zircon. With the trace element composition of zircon increasingly being used to interpret conditions of primary zircon crystallisation (e.g., Grimes et al., 2015; Loucks et al., 2020), this may then lead to erroneous interpretations from zircon chemistry. For example, Ti in zircon is widely used as an igneous thermometer, yet the BRM zircons span a huge range of Ti contents, from <10 ppm to >1000 ppm (Fig. 6b). Using the Ti-in-zircon thermometer of Watson et al. (2006) and assuming an activity of $TiO_2 = 1$, these Ti contents would correspond to crystallisation temperatures of ~700 °C to over >1400 °C; the latter of which is clearly unrealistically high for zircon crystallisation in crustal rocks. The BRM zircons are likely an extreme case, but nonetheless it is prudent to carefully consider potential chemical modification of zircon following radiation damage, prior to interpreting primary crystallisation conditions from the trace element composition of the zircon.

5.3. Timing of 'non-formula' element uptake in metamict BRM zircon

Constraining when non-formula elements such as REE were sequestered into the metamict BRM zircon is crucial for evaluating the role of BRM zircon as a source of metals for unconformity-related REE mineralisation at Browns Range. A first order constraint is that the zircon structure needs to be sufficiently radiation damaged to allow incorporation of these non-formula elements. Using the age (i.e., ca. 3.1 Ga; Nazari-Dehkordi et al., 2017) and original Th and U contents of the BRM zircons (taken from the least altered zircon domains), we have calculated the α radiation dose evolution of the BRM zircons through time, using the formulation of Holland and Gottfried (1955). The modelled radiation dose evolution (Fig. 11) indicates that these zircons would have reached the percolation threshold, i.e., the interconnection of aperiodic domains throughout the crystal structure (Ewing et al., 2003) by ~2.6 Ga, assuming minimal structural annealing during this period. Once the percolation threshold is exceeded, the zircon grains are open to fluid infiltration/reaction, and can take up non-formula elements.

We consider three potential events of element uptake during the geological history of the Browns Range zircon: (i) element uptake during pre 2.5 Ga sedimentary deposition of the BRM (labelled 1 on Fig. 11); (ii) element uptake during regional metamorphism between ca. 1.83 and 1.72 Ga (labelled 2 on Fig. 11); and (iii) element uptake during modern exposure and weathering (labelled 3 on Fig. 11). Although modern weathering has been proposed as a mechanism for element uptake in metamict zircon (Delattre et al., 2007; Hay and Dempster, 2009b), most of the samples examined here are drillcore samples derived from ~100 m or ~ 441 m below the surface, which is well below the weathering zone. Therefore, the bulk of non-formula element uptake cannot be due to modern surface weathering processes. Sample NM1 was the only sample collected from a surface outcrop, and does have a distinct zircon composition with relatively high Fe, Al, Nb, P, and variable Y + REE contents (Figs. 6 and 7). These specific features may be attributed to modern weathering, and ultimately could contribute to understanding the behaviour of trace elements in low temperature weathering environments (e.g., Jowitt et al., 2017).

Element uptake in zircon, due to hydrothermal alteration related to ca. 1.8 Ga regional metamorphism (Crispe et al., 2007), would be consistent with the hydrothermal model proposed by Geisler et al. (2003b) for hydrated metamict zircons rich in trace elements from the Eastern Desert, Egypt. For Browns Range, elements sequestered in zircon may be sourced via metamorphic reactions involving the breakdown of phases such as titanite, chlorite, and apatite, although this is largely speculation as there is little information on the nature of this metamorphic event. It is likely, however, that metamorphic conditions exceeded the thermal limits for zircon annealing (~300 °C), which would tend to inhibit trace element uptake in zircon due to structural recovery (Härtel et al., 2021).

Our preferred scenario for trace element uptake by the metamict BRM zircon is during original sedimentary deposition of the BRM, likely around 2.5 to 2.6 Ga (labelled 1 on Fig. 11). Continental weathering and erosion during the Late Archean operated within a high-CO_2, relatively low-pH atmosphere (Catling and Zahnle, 2020). These are the conditions that would have favoured complete breakdown of any detrital apatite (Hao et al., 2020a; Hao et al., 2020b) and titanite (Novoselov et al., 2020) during surface weathering, which provides an explanation for the lack of these phases in the BRM. These phases are also important repositories for REE, Y, Th, U, P, Ca, Nb, and Ti (Hammerli and Kemp, 2021; Hammerli et al., 2016), therefore their breakdown would have allowed redistribution of these elements into metamict zircon. The timing of non-formula element uptake by zircon is difficult to determine directly, as element uptake is expected to disturb isotopic geochronometers such as the U—Pb system. Previous U—Pb age dating by

Nazari-Dehkordi et al. (2017) produced a ca. 3.1 Ga primary age for the BRM zircons, but these authors specifically targeted zircon domains with minimal radiation damage. We have acquired a more comprehensive U—Pb geochronology dataset for the BRM zircons examined here, including on highly-metamict grain domains (see Appendix 2). The vast majority of our analyses are highly discordant (>30% discordance), consistent with variable levels of recent Pb loss. The discordant analyses are likely on metamict zircon domains, as metamict zircons are known to be susceptible to Pb loss (e.g., Nasdala et al., 2001b), and we observe a clear correlation between U (and Th) contents of zircon and the degree of discordance (see Appendix 2; Fig. A2.1). On a Concordia diagram (Appendix 2; Fig. A2.2) these discordant data plot within a field defined by discordia arrays between the zero age and ca. 3.1 Ga (primary zircon crystallisation age) and ca. 1.6 Ga (REE mineralisation age), with an intermediate array between zero and ca. 2.6 Ga, the latter age interpreted to be the timing of sedimentation of the BRM and non-formula element uptake in metamict zircon.

The uptake of non-formula elements into the metamict zircon includes substantial amounts (up to wt% levels) of Th and U, which in turn will further exacerbate radiation damage in the zircon. We have modelled the radiation dose evolution of these Th + U enriched zircon domains for the various scenarios of elemental uptake discussed above (shown as red curves in Fig. 11). These radiation dose trends project to very high radiation dose levels at the present day (~5 to 8.5 × 10^{19} α-decays/g; Fig. 11), which is consistent with the extensively damaged and amorphous nature of the BRM zircons, as revealed from our chemical, Raman, and crystal structure results.

5.4. *Mobilisation of 'non-formula' elements from metamict BRM zircon, and implications for unconformity-related HREE mineralisation*

Leaching experiments with saline fluids demonstrate that the solubility of, and element mobility from, metamict zircon are several orders of magnitude higher than for pristine zircon (Ewing et al., 2003; Geisler et al., 2003a), especially at dose rates above 3.5 × 10^{18} α-decays/g (Ewing et al., 2003; Fig. 11). We suggest that significant levels of REE can be leached from zircon by saline fluids under these conditions (Geisler et al., 2003a). However, a crucial aspect of the conditions for ore formation is that the ore fluids remained below ~300 °C. At higher temperatures, the element solubility capacity of the saline fluids is likely to be higher (e.g., Migdisov et al., 2016), but the zircons will undergo thermal annealing or structural recovery (Härtel et al., 2021), thereby 'locking' away its contained REEs from fluid leaching. This concept of an effective 'temperature ceiling' for ore formation processes is somewhat counter-intuitive, as increasing temperature is often regarded to have a direct and primary control on the element transport capacity of hydrothermal fluids. In this case, remaining below the ~300 °C temperature ceiling is crucial, not only at the time of hydrothermal fluid flow, but also for at least 100 m.y. *prior* to ore formation to ensure that the zircon remains in a metamict (and hence fluid soluble) state above the percolation threshold (Fig. 11) during the fluid alteration event. With this in mind, an understanding of thermal histories is a key criterion for assessing regional prospectivity for unconformity-related REE mineralisation.

Demonstrably, the REE for the unconformity-related mineralisation at Browns Range were sourced from the BRM (Nazari-Dehkordi et al., 2018; Nazari-Dehkordi et al., 2020), and zircon is the primary host (60–90%) of Y + HREE in the BRM (Fig. 2). Hydrothermal xenotime mineralisation formed from REE-bearing, high-salinity (up to 25 wt%) fluids at temperatures of 100 to 250 °C (Nazari-Dehkordi et al., 2019). Mineralisation occurred at 1.65 to 1.60 Ga (Nazari-Dehkordi et al., 2018; Nazari-Dehkordi et al., 2020), at which time the BRM zircons would have experienced extensive levels of radiation damage (orange stars on Fig. 11), regardless of when non-formula element uptake by zircon had occurred (i.e., either case 1 or 2 in Fig. 11). In all cases, the BRM zircon would have been highly amenable to element leaching at this time, as temperature conditions were too low (i.e., < 300 °C) to allow for the annealing of the zircon grains. Therefore, we propose that Y + REE were leached from metamict zircon in the BRM by circulating saline brines, which then precipitated the REE ore minerals xenotime (and minor florencite) in fault zones and along the unconformity surface during fluid cooling and/or mixing (Nazari-Dehkordi et al., 2018; Nazari-Dehkordi et al., 2020).

Detailed investigation of the process of fluid leaching for metamict zircon is beyond the scope of this study. Nonetheless, the quartz-sericite shear zone formed by extensive fluid alteration (sample W5–11), contains metamict, non-formula element rich zircon domains that are rimmed by a pristine, or 'clean' zircon generation (Fig. 3F) that is largely devoid of non-formula elements (from EDS analysis). We interpret this new zircon rim to represent the residual product of fluid alteration of the metamict zircon, with the 'non-formula' element components (e.g., REE, Y and P), removed by the altering hydrothermal fluids. These zircons, therefore, may record the grain-scale fluid reaction processes that leads to REE transport by saline fluids. Research work is underway to investigate these processes further.

The experiments of Geisler et al. (2003a) demonstrate that between 60 and 80% of REE can be leached from metamict zircon by saline fluids at temperatures between 175 and 350 °C. If we assume a modest leaching efficiency of 10%, then the fluid infiltration and leaching of a rock volume of approximately 1 km^3 of BRM (with ~270 ppm Y + REE; Nazari-Dehkordi et al., 2017) would be required to mobilise all of the ~81,000 t of total REE oxide (TREO) mineralisation currently recognised within the Browns Range Dome (Northern Minerals Ltd, 2022). This volume of leached rock from the BRM is plausible, as the mineralisation is spread over an exposed area of ~100 km^2 (Fig. 1), and the BRM extends to at least 500 m depth (as confirmed by drilling at the Wolverine Deposit; Northern Minerals Ltd, 2022).

The HREE-rich nature of the Browns Range REE deposits stands as a conundrum as HREE are expected to be significantly less mobile in most hydrothermal fluids than LREE (Haas et al., 1995; Migdisov et al., 2016). Sourcing REE from metamict zircon represents a neat resolution to this enigma, as the zircon itself is enriched in HREE over LREE (Fig. 7), so there is no requirement for significant fractionation of REE during fluid leaching or ore deposition in this case. Indeed, many of the geochemical characteristics of the REE ores at Browns Range closely resemble the compositions of the BRM zircons (Fig. 7F, Fig. 12), indicating limited element fractionation during fluid leaching, migration, and ore formation. Among the exceptions are low contents of Th, U, and Zr in the ores (Fig. 12 B, D), which we suggest may be due to relative immobility of quadrivalent cations (compared to trivalent REE) during saline fluid leaching (e.g., Nisbet et al., 2018).

Previous studies have suggested that the P and REE required for the xenotime (and minor florencite) mineralisation were derived from difference sources (Nazari-Dehkordi et al., 2018; Nazari-Dehkordi et al., 2020), with REE from the BRM, and the P from the overlying Gardiner Sandstone (base of the Birrindudu Basin), despite there being no currently recognised P source within this unit. The rationale for this model is that REE phosphates are too insoluble to be transported together in low T hydrothermal fluids (Gysi et al., 2015; Louvel et al., 2015; Migdisov et al., 2016), such that fluid mixing in fault zones or along the unconformity surface would be an efficient mechanism by which to precipitate ore minerals (Nazari-Dehkordi et al., 2018; Nazari-Dehkordi et al., 2020). Our new data show that the P:REE values of the BRM zircon and REE ores are similar (Fig. 12E, F), which would support an alternative premise that both the REE and P for the mineralisation were derived from the BRM zircons. Low pH saline fluids could have transported these components as $REECl^{2+}$ or $REECl_2^+$ and $H_2(PO_4)^-$, respectively (Gysi et al., 2015; Hao et al., 2020a; Hao et al., 2020b; Migdisov et al., 2016), though further work is required to evaluate the solubility and species stability in fluids leaching zircon at low temperature (< 300 °C).

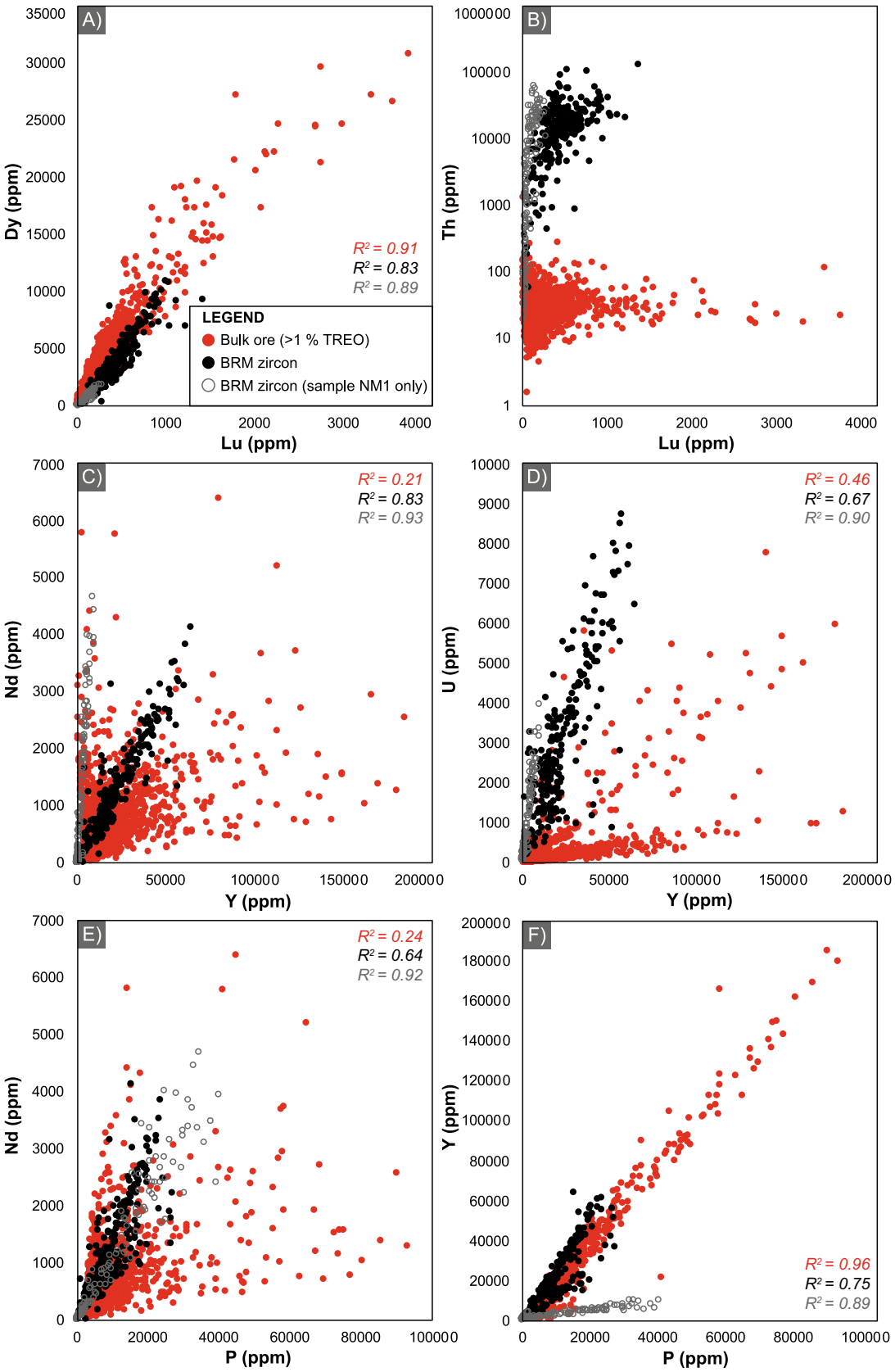

Fig. 12. BRM zircon (black) versus bulk ore (red; >1% total rare earth oxide; TREO) trace element binary plots (in ppm). (a) Lutetium versus Dy. (b) Lutetium versus Th. (c) Yttrium versus Nd. (d) Yttrium versus U. (e) Phosphorus versus Nd. (f) Phosphorus versus Y. Bulk ore data ($n = 2673$, whereas for P $n = 1496$) from Northern Minerals Ltd. (2022). (For interpretation of the references to colour in this figure legend, the reader is referred to the web version of this article.)

6. Conclusions

Archean zircon from the arkosic metasediments of the BRM have unusual compositions (high non-formula element contents: U, Th, Y, REE, Nb, P, Al, Ca, Fe, Ti, F, and OH^- or H_2O), and structural features (porous and amorphous domains, cavities and voids) that are consistent with extensive radiation damage, followed by uptake of non-formula elements during weathering and sediment deposition. These zircons host the majority of HREE inventory of these rocks, and are herein demonstrated to be the source of REE for local unconformity-related HREE ore deposits. Based on our data and the regional geological history, we outline a sequence of events that led to ore formation:

(1) Zircons from a Mesoarchean granitic source region were subject to radiation damage and metamictisation between ca. 3.1 and 2.6 Ga.
(2) Weathering and erosion of the granitic source during the late Archean (possibly under high CO_2-rich, relatively low pH surface conditions), led to the breakdown of detrital apatite and/or titanite, with REE, P, Th, and U liberated from these phases and sequestered into metamict zircons as 'non-formula' elements. The relatively short transport distance of these sediments led to deposition of the arkosic BRM, without extensive mechanical breakdown of zircon.
(3) BRM zircons, now with elevated Th and U contents, evolved to a state of extreme radiation damage. Metamictisation is sustained due to a lack of thermal annealing across the Late Archean into the Paleoproterozoic.
(4) Regional metamorphism at ca. 1.8 to 1.7 Ga may have partially annealed the zircons, or may have allowed further non-formula element uptake, or both.
(5) Pervasive circulation of saline basinal brines at ca. 1.65 to 1.62 Ga allowed leaching of REE and possibly P from the metamict zircons. Migration of these element-laden fluids into fault zones or along the overlying unconformity led to ore formation. Fluid mixing in these locations was likely a key driver for REE ore mineral precipitation (Nazari-Dehkordi et al., 2019). Importantly, the fluid temperature remained below the temperature ceiling of ~300 °C, preventing thermal annealing of the metamict zircons.

This model for ore formation provides an elegant explanation for why these deposits are HREE rich, and why they are dispersed across the Browns Range Dome (Fig. 1). We suspect similar ore genesis processes were responsible for unconformity-related, HREE mineralisation at John Galt, Mount Mansbridge, and Watts Rise-Castella (also known as Killi Killi Hills) Australia; (Fig. 1), and the Maw Zone, Athabasca Basin, Canada (Rabiei et al., 2017), all of which are associated with Archean to Paleoproterozoic clastic sedimentary rocks that likely contain metamict detrital zircon (Card et al., 2007; Cross and Crispe, 2007). More broadly, fluid leaching from metamict zircon may be an important metal source for other basin hosted ore deposits, including unconformity U and orogenic U ore deposits (e.g., McGloin et al., 2016; Sun et al., 2021). In this case mineral exploration would be enhanced by comprehensive knowledge of the age and thermal history of basins and detailed understanding of regimes of hydrothermal fluid flow through, within and between (i.e., across unconformities or structural breaks) basin systems.

Declaration of Competing Interest

The authors declare that they have no known competing financial interests or personal relationships that could have appeared to influence the work reported in this paper.

Data availability

Data will be made available on request.

Acknowledgements

This research was supported by ARC Linkage Project (LP190100635). The authors acknowledge the scientific and technical assistance of Dr. Sarah Gilbert (LA-ICP-MS), Dr. Benjamin Wade (EPMA), Dr. Ashley Slattery (STEM) and Dr. Animesh Basak (FIB-SEM) at Adelaide Microscopy, The University of Adelaide. The authors acknowledge the detailed and constructive comments of Prof. Daniel Harlov (GFZ Potsdam) and two anonymous reviewers. Prof. Balz Kamber is thanked for editorial handling of the manuscript.

Appendix A. Supplementary data

Supplementary data to this article can be found online at https://doi.org/10.1016/j.chemgeo.2023.121493.

References

Ahmad, M., Vandenberg, L., Wygralak, A., Munson, T., 2013. Tanami Region. Geology and Mineral Resources of the Northern Territory. Northern Territory Geological Survey, Special Publication, 5, pp. 11.1–11.41.
Ali, S.H., et al., 2017. Mineral supply for sustainable development requires resource governance. Nature 543 (7645), 367–372. https://doi.org/10.1038/nature21359.
Anenburg, M., Williams, M.J., 2022. Quantifying the tetrad effect, shape components, and Ce–Eu–Gd anomalies in rare earth element patterns. Math. Geosci. 54 (1), 47–70. https://doi.org/10.1007/s11004-021-09959-5.
Blake, D.H., Tyler, I.M., Warren, R.G., 2000. Gordon Downs, Western Australia - 1:250 000 Geological Series (Second Edition) SE52–10, Australian Geological Survey Organisation.
Broska, I., Williams, C.T., Uher, P., Konečný, P., Leichmann, J.r., 2004. The geochemistry of phosphorus in different granite suites of the Western Carpathians, Slovakia: the role of apatite and P-bearing feldspar. Chem. Geol. 205 (1–2), 1–15. https://doi.org/10.1016/j.chemgeo.2003.09.004.
Bruce, S., et al., 2021. Critical Energy Minerals Roadmap. CSIRO.
Card, C., et al., 2007. Basement rocks to the Athabasca basin, Saskatchewan and Alberta. Bulletin-Geological Survey of Canada 588, 69.
Catling, D.C., Zahnle, K.J., 2020. The Archean Atmosphere. Science. Advances 6 (9), eaax1420. https://doi.org/10.1126/sciadv.aax1420.
Chakoumakos, B.C., Murakami, T., Lumpkin, G.R., Ewing, R.C., 1987. Alpha-decay induced fracturing in zircon: the transition from the crystalline to the metamict state. Science 236 (4808), 1556–1559. https://doi.org/10.1126/science.236.4808.1556.
Cherniak, D.J., Watson, E.B., 2003. Diffusion in zircon. Rev. Mineral. Geochem. 53 (1), 113–143. https://doi.org/10.2113/0530113.
Ciobanu, C., Cook, N., Utsunomiya, S., Pring, A., Green, L., 2011. Focussed ion beam–transmission electron microscopy applications in ore mineralogy: Bridging micro-and nanoscale observations. Ore Geol. Rev. 42 (1), 6–31. https://doi.org/10.1016/j.oregeorev.2011.06.012.
Collins, W., Beams, S., White, A., Chappell, B., 1982. Nature and origin of A-type granites with particular reference to southeastern Australia. Contrib. Mineral. Petrol. 80 (2), 189–200. https://doi.org/10.1007/BF00374895.
Crispe, A., Vandenberg, L., Scrimgeour, I., 2007. Geological framework of the Archean and Paleoproterozoic Tanami Region, Northern Territory. Mineralium Deposita 42 (1), 3–26. https://doi.org/10.1007/s00126-006-0107-1.
Cross, A., Crispe, A., 2007. SHRIMP U–Pb analyses of detrital zircon: a window to understanding the Paleoproterozoic development of the Tanami Region, northern Australia. Mineral. Deposita 42 (1), 27–50. https://doi.org/10.1007/s00126-006-0102-6.
Dawson, P., Hargreave, M., Wilkinson, G., 1971. The vibrational spectrum of zircon ($ZrSiO_4$). J. Phys. C Solid State Phys. 4 (2), 240. https://doi.org/10.1088/0022-3719/4/2/014.
Delattre, S., et al., 2007. Dissolution of radiation-damaged zircon in lateritic soils. Am. Mineral. 92 (11−12), 1978–1989. https://doi.org/10.2138/am.2007.2514.
Ewing, R.C., Meldrum, A., Wang, L., Weber, W.J., Corrales, L.R., 2003. Radiation effects in zircon. Rev. Mineral. Geochem. 53 (1), 387–425. https://doi.org/10.2113/0530387.
Finch, R.J., Hanchar, J.M., 2003. Structure and chemistry of zircon and zircon-group minerals. Rev. Mineral. Geochem. 53 (1), 1–25. https://doi.org/10.2113/0530001.
Finch, R.J., Hanchar, J.M., Hoskin, P.W., Burns, P.C., 2001. Rare-earth elements in synthetic zircon: part 2. A single-crystal X-ray study of xenotime substitution. Am. Mineral. 86 (5–6), 681–689. https://doi.org/10.2138/am-2001-5-608.
Gain, S.E., et al., 2019. Mud Tank Zircon: long-term evaluation of a reference material for U-Pb dating, Hf-isotope analysis and trace element analysis. Geostand. Geoanal. Res. 43 (3), 339–354. https://doi.org/10.1111/ggr.12265.
Geisler, T., Pidgeon, R., Van Bronswijk, W., Kurtz, R., 2002. Transport of uranium, thorium, and lead in metamict zircon under low-temperature hydrothermal

conditions. Chem. Geol. 191 (1–3), 141–154. https://doi.org/10.1016/S0009-2541(02)00153-5.
Geisler, T., Pidgeon, R.T., Kurtz, R., Van Bronswijk, W., Schleicher, H., 2003a. Experimental hydrothermal alteration of partially metamict zircon. Am. Mineral. 88 (10), 1496–1513. https://doi.org/10.2138/am-2003-1013.
Geisler, T., et al., 2003b. Low-temperature hydrothermal alteration of natural metamict zircons from the Eastern Desert, Egypt. Mineralogical Magazine 67 (3), 485–508. https://doi.org/10.1180/0026461036730112.
Geisler, T., Schaltegger, U., Tomaschek, F., 2007. Re-equilibration of zircon in aqueous fluids and melts. Elements 3 (1), 43–50. https://doi.org/10.2113/gselements.3.1.43.
Grimes, C., Wooden, J., Cheadle, M., John, B., 2015. "Fingerprinting" tectono-magmatic provenance using trace elements in igneous zircon. Contrib. Mineral. Petrol. 170 (5), 1–26. https://doi.org/10.1007/s00410-015-1199-3.
Gysi, A.P., Williams-Jones, A.E., Harlov, D., 2015. The solubility of xenotime-(Y) and other HREE phosphates in aqueous solutions from 100 to 250 °C and p_{sat}. Chem. Geol. 401, 83–95. https://doi.org/10.1016/j.chemgeo.2015.02.023.
Haas, J.R., Shock, E.L., Sassani, D.C., 1995. Rare earth elements in hydrothermal systems: estimates of standard partial molal thermodynamic properties of aqueous complexes of the rare earth elements at high pressures and temperatures. Geochim. Cosmochim. Acta 59 (21), 4329–4350. https://doi.org/10.1016/0016-7037(95)00314-P.
Hammerli, J., Kemp, A.I., 2021. Combined Hf and Nd isotope microanalysis of co-existing zircon and REE-rich accessory minerals: High resolution insights into crustal processes. Chem. Geol. 581, 120393 https://doi.org/10.1016/j.chemgeo.2021.120393.
Hammerli, J., Spandler, C., Oliver, N.H., 2016. Element redistribution and mobility during upper crustal metamorphism of metasedimentary rocks: an example from the eastern Mount Lofty Ranges, South Australia. Contrib. Mineral. Petrol. 171 (4), 1–21. https://doi.org/10.1007/s00410-016-1239-7.
Hanchar, J.M., et al., 2001. Rare earth elements in synthetic zircon: part 1. Synthesis, and rare earth element and phosphorus doping. Am. Mineral. 86 (5–6), 667–680. https://doi.org/10.2138/am-2001-5-607.
Hao, J., Knoll, A.H., Huang, F., Hazen, R.M., Daniel, I., 2020a. Cycling phosphorus on the Archean Earth: part I. Continental weathering and riverine transport of phosphorus. Geochim. Cosmochim. Acta 273, 70–84. https://doi.org/10.1016/j.gca.2020.01.027.
Hao, J., et al., 2020b. Cycling phosphorus on the Archean Earth: Part II. Phosphorus limitation on primary production in Archean ecosystems. Geochim. Cosmochim. Acta 280, 360–377. https://doi.org/10.1016/j.gca.2020.04.005.
Harlavan, Y., Erel, Y., 2002. The release of Pb and REE from granitoids by the dissolution of accessory phases. Geochim. Cosmochim. Acta 66 (5), 837–848. https://doi.org/10.1016/S0016-7037(01)00806-7.
Härtel, B., Jonckheere, R., Wauschkuhn, B., Ratschbacher, L., 2021. The closure temperature(s) of zircon Raman dating. Geochronology 3 (1), 259–272. https://doi.org/10.5194/gchron-3-259-2021.
Hay, D., Dempster, T., 2009a. Zircon behaviour during low-temperature metamorphism. J. Petrol. 50 (4), 571–589. https://doi.org/10.1093/petrology/egp047.
Hay, D.C., Dempster, T.J., 2009b. Zircon alteration, formation and preservation in sandstones. Sedimentology 56 (7), 2175–2191. https://doi.org/10.1111/j.1365-3091.2009.01075.x.
Hermann, J., 2002. Allanite: thorium and light rare earth element carrier in subducted crust. Chem. Geol. 192 (3–4), 289–306. https://doi.org/10.1016/S0009-2541(02)00222-X.
Holland, H.D., Gottfried, D., 1955. The effect of nuclear radiation on the structure of zircon. Acta Crystallogr. 8 (6), 291–300. https://doi.org/10.1107/S0365110X55000947.
Hoskin, P.W., 2005. Trace-element composition of hydrothermal zircon and the alteration of Hadean zircon from the Jack Hills, Australia. Geochimica et Cosmochimica Acta 69 (3), 637–648. https://doi.org/10.1016/j.gca.2004.07.006.
Hoskin, P.W., Schaltegger, U., 2003. The composition of zircon and igneous and metamorphic petrogenesis. Rev. Mineral. Geochem. 53 (1), 27–62. https://doi.org/10.2113/0530027.
Jowitt, S.M., Wong, V.N.L., Wilson, S., Gore, O., 2017. Critical metals in the critical zone: controls, resources and future prospectivity of regolith-hosted rare earth elements. Aust. J. Earth Sci. 64 (8), 1045–1054. https://doi.org/10.1080/08120099.2017.1380701.
Kirkland, C., Smithies, R., Taylor, R., Evans, N., McDonald, B., 2015. Zircon Th/U ratios in magmatic environs. Lithos 212, 397–414. https://doi.org/10.1016/j.lithos.2014.11.021.
Kolesov, B., 2006. Raman investigation of H_2O molecule and hydroxyl groups in the channels of hemimorphite. Am. Mineral. 91 (8–9), 1355–1362. https://doi.org/10.2138/am.2006.2179.
Kolesov, B.A., Geiger, C.A., Armbruster, T., 2001. The dynamic properties of zircon studied by single-crystal X-ray diffraction and Raman spectroscopy. Eur. J. Mineral. 13 (5), 939–948. https://doi.org/10.1127/0935-1221/2001/0013-0939.
Loucks, R.R., Fiorentini, M.L., Henríquez, G.J., 2020. New magmatic oxybarometer using trace elements in zircon. J. Petrol. 61 (3), egaa034. https://doi.org/10.1093/petrology/egaa034.
Louvel, M., Bordage, A., Testemale, D., Zhou, L., Mavrogenes, J., 2015. Hydrothermal controls on the genesis of REE deposits: Insights from an *in situ* XAS study of Yb solubility and speciation in high temperature fluids (T < 400° C). Chem. Geol. 417, 228–237. https://doi.org/10.1016/j.chemgeo.2015.10.011.
Lv, J., Li, G., Guo, S., Shi, Y., 2016. Raman scattering from phonons and electronic excitations in UO2 with different oxygen isotopes. J. Raman Spectrosc. 47 (3), 345–349. https://doi.org/10.1002/jrs.4785.
Ma, Y., Li, N., Xiang, S., Guan, N., 2007. IR and Raman investigation of one-dimensional and three-dimensional aluminophosphite. J. Phys. Chem. C 111 (49), 18361–18366. https://doi.org/10.1021/jp0763679.
Maidment, D.W., et al., 2020. Geochronology of Metasedimentary and Granitic Rocks in the Granites-Tanami Orogen: 1885–1790 Ma Geodynamic Evolution. Geological Survey of Western Australia.
McGloin, M.V., et al., 2016. Release of uranium from highly radiogenic zircon through metamictization: the source of orogenic uranium ores. Geology 44 (1), 15–18. https://doi.org/10.1130/G37238.1.
McMillan, P.F., 1989. Raman spectroscopy in mineralogy and geochemistry. Annu. Rev. Earth Planet. Sci. 17, 255. https://doi.org/10.1146/annurev.ea.17.050189.001351.
Meldrum, A., Boatner, L.A., Weber, W.J., Ewing, R.C., 1998. Radiation damage in zircon and monazite. Geochim. Cosmochim. Acta 62 (14), 2509–2520. https://doi.org/10.1016/S0016-7037(98)00174-4.
Mezger, K., Krogstad, E., 1997. Interpretation of discordant U-Pb zircon ages: an evaluation. J. Metamorph. Geol. 15 (1), 127–140. https://doi.org/10.1111/j.1525-1314.1997.00008.x.
Migdisov, A., Williams-Jones, A., Brugger, J., Caporuscio, F.A., 2016. Hydrothermal transport, deposition, and fractionation of the REE: Experimental data and thermodynamic calculations. Chem. Geol. 439, 13–42. https://doi.org/10.1016/j.chemgeo.2016.06.005.
Morin-Ka, S., et al., 2016. Alteration and age of the Browns Range heavy rare earth element deposits. In: GSWA 2016 Extended Abstracts: Promoting the Prospectivity of Western Australia: Geological Survey of Western Australia Record, 2, pp. 21–25.
Murakami, T., Chakoumakos, B.C., Ewing, R.C., Lumpkin, G.R., Weber, W.J., 1991. Alpha-decay event damage in zircon. Am. Mineral. 76 (9–10), 1510–1532.
Nasdala, L., Irmer, G., Wolf, D., 1995. The degree of metamictization in zircon: a Raman spectroscopic study. Eur. J. Mineral. 471-478 https://doi.org/10.1127/ejm/7/3/0471.
Nasdala, L., Beran, A., Libowitzky, E., Wolf, D., 2001a. The incorporation of hydroxyl groups and molecular water in natural zircon ($ZrSiO_4$). Am. J. Sci. 301 (10), 831–857. https://doi.org/10.2475/ajs.301.10.831.
Nasdala, L., et al., 2001b. Metamictisation of natural zircon: accumulation versus thermal annealing of radioactivity-induced damage. Contrib. Mineral. Petrol. 141 (2), 125–144. https://doi.org/10.1007/s004100000235.
Nasdala, L., et al., 2004. Incomplete retention of radiation damage in zircon from Sri Lanka. Am. Mineral. 89 (1), 219–231. https://doi.org/10.2138/am-2004-0126.
Nazari-Dehkordi, T., Spandler, C., 2019. Paragenesis and composition of xenotime-(Y) and florencite-(Ce) from unconformity-related heavy rare earth element mineralization of northern Western Australia. Mineral. Petrol. 113 (5), 563–581. https://doi.org/10.1007/s00710-019-00676-w.
Nazari-Dehkordi, T., Spandler, C., Oliver, N., Chapman, J., Wilson, R., 2017. Provenance, tectonic setting and source of Archean metasedimentary rocks of the Browns Range Metamorphics, Tanami Region, Western Australia. Aust. J. Earth Sci. 64 (6), 723–741. https://doi.org/10.1080/08120099.2017.1355844.
Nazari-Dehkordi, T., Spandler, C., Oliver, N.H., Wilson, R., 2018. Unconformity-related rare earth element deposits: a regional-scale hydrothermal mineralization type of Northern Australia. Econ. Geol. 113 (6), 1297–1305. https://doi.org/10.5382/econgeo.2018.4592.
Nazari-Dehkordi, T., Huizenga, J.M., Spandler, C., Oliver, N.H., 2019. Fluid inclusion and stable isotope constraints on the heavy rare earth element mineralisation in the Browns Range Dome, Tanami Region, Western Australia. Ore Geology Reviews 113, 103068. https://doi.org/10.1016/j.oregeorev.2019.103068.
Nazari-Dehkordi, T., Spandler, C., Oliver, N.H., Wilson, R., 2020. Age, geological setting, and paragenesis of heavy rare earth element mineralization of the Tanami region, Western Australia. Mineralium Deposita 55 (1), 107–130. https://doi.org/10.1007/s00126-019-00878-4.
Nisbet, H., Migdisov, A., Xu, H., Guo, X., van Hinsberg, V., Williams-Jones, A.E., Boukhalfa, H., Roback, R., 2018. An experimental study of the solubility and speciation of thorium in chloride-bearing aqueous solutions at temperatures up to 250 C. Geochim. Cosmochim. Acta 239, 363–373. https://doi.org/10.1016/j.gca.2018.08.001.
Northern Minerals Ltd, 2022. Quarterly Activities Report: September 2022, Northern Minerals Ltd. (ASX: NTU): ASX Announcements.
Novoselov, A.A., Silva, D., de Souza Filho, C.R., 2020. Authigenic titanite in weathered basalts: Implications for paleoatmospheric reconstructions. Geosci. Front. 11 (6), 2183–2196. https://doi.org/10.1016/j.gsf.2020.03.012.
Palenik, C.S., Nasdala, L., Ewing, R.C., 2003. Radiation damage in zircon. Am. Mineral. 88 (5–6), 770–781. https://doi.org/10.2138/am-2003-5-606.
Palme, H., O'Neill, H., 2014. Cosmochemical estimates of mantle composition. In: Treatise on Geochemistry (Second Edition), 3: The Mantle and Core, pp. 1–39.
Pidgeon, R.T., Nemchin, A.A., Roberts, M.P., Whitehouse, M.J., Bellucci, J.J., 2019. The accumulation of non-formula elements in zircons during weathering: Ancient zircons from the Jack Hills, Western Australia. Chemical Geology 530, 119310. https://doi.org/10.1016/j.chemgeo.2019.119310.
Rabiei, M., et al., 2017. Hydrothermal rare earth element (xenotime) mineralization at Maw Zone, Athabasca Basin, Canada, and its relationship to unconformity-related uranium deposits. Econ. Geol. 112 (6), 1483–1507. https://doi.org/10.5382/econgeo.2017.4518.
Reddy, S.M., et al., 2006. Crystal-plastic deformation of zircon: a defect in the assumption of chemical robustness. Geology 34 (4), 257–260. https://doi.org/10.1130/G22110.1.
Rubatto, D., 2002. Zircon trace element geochemistry: partitioning with garnet and the link between U–Pb ages and metamorphism. Chem. Geol. 184 (1–2), 123–138. https://doi.org/10.1016/S0009-2541(01)00355-2.

Sergeeva, A.V., Zhitova, E.S., Bocharov, V.N., 2019. Infrared and Raman spectroscopy of tschermigite, $(NH_4)Al(SO_4)_2{\cdot}12H_2O$. Vib. Spectrosc. 105, 102983 https://doi.org/10.1016/j.vibspec.2019.102983.

Shibata, N., Horigudhi, M., Edahiro, T., 1981. Raman spectra of binary high-silica glasses and fibers containing GeO_2, P_2O_5 and B_2O_3. J. Non-Cryst. Solids 45 (1), 115–126. https://doi.org/10.1016/0022-3093(81)90096-X.

Spandler, C., Pirard, C., 2013. Element recycling from subducting slabs to arc crust: a review. Lithos 170, 208–223. https://doi.org/10.1016/j.lithos.2013.02.016.

Spandler, C., Hermann, J., Arculus, R., Mavrogenes, J., 2003. Redistribution of trace elements during prograde metamorphism from lawsonite blueschist to eclogite facies; implications for deep subduction-zone processes. Contrib. Mineral. Petrol. 146 (2), 205–222. https://doi.org/10.1007/s00410-003-0495-5.

Spandler, C., Slezak, P., Nazari-Dehkordi, T., 2020. Tectonic significance of Australian rare earth element deposits. Earth Sci. Rev. 207, 103219 https://doi.org/10.1016/j.earscirev.2020.103219.

Sun, Y., Wu, L., Jiao, Y., Rong, H., Zhang, F., 2021. Alteration and elements migration of detrital zircons from the Daying uranium deposit in the Ordos Basin, China. Ore Geol. Rev. 139, 104418. https://doi.org/10.1016/j.oregeorev.2021.104418.

Syme, R., Lockwood, D., Kerr, H., 1977. Raman spectrum of synthetic zircon ($ZrSiO_4$) and thorite ($ThSiO_4$). J. Phys. C Solid State Phys. 10 (8) https://doi.org/10.1088/0022-3719/10/8/036.

Thomas, S.-M., et al., 2009. IR calibrations for water determination in olivine, r-GeO_2, and SiO_2 polymorphs. Phys. Chem. Miner. 36 (9), 489–509. https://doi.org/10.1007/s00269-009-0295-1.

Trocellier, P., Delmas, R., 2001. Chemical durability of zircon. Nucl. Instrum. Methods Phys. Res., Sect. B 181 (1–4), 408–412. https://doi.org/10.1016/S0168-583X(01)00377-9.

Valley, J.W., et al., 2014. Hadean age for a post-magma-ocean zircon confirmed by atom-probe tomography. Nat. Geosci. 7 (3), 219–223. https://doi.org/10.1038/ngeo2075.

Watson, E., Wark, D., Thomas, J., 2006. Crystallization thermometers for zircon and rutile. Contrib. Mineral. Petrol. 151 (4), 413–433. https://doi.org/10.1007/s00410-006-0068-5.

Whalen, J.B., Currie, K.L., Chappell, B.W., 1987. A-type granites: geochemical characteristics, discrimination and petrogenesis. Contrib. Mineral. Petrol. 95 (4), 407–419. https://doi.org/10.1007/BF00402202.

Wilde, S.A., Valley, J.W., Peck, W.H., Graham, C.M., 2001. Evidence from detrital zircons for the existence of continental crust and oceans on the Earth 4.4 Gyr ago. Nature 409 (6817), 175–178. https://doi.org/10.1038/35051550.

Williams-Jones, A., 2015. The hydrothermal mobility of the rare earth elements. British Columbia Geological Survey, Paper 3, 119–123.

Wirth, R., 2009. Focused Ion Beam (FIB) combined with SEM and TEM: Advanced analytical tools for studies of chemical composition, microstructure and crystal structure in geomaterials on a nanometre scale. Chem. Geol. 261 (3–4), 217–229. https://doi.org/10.1016/j.chemgeo.2008.05.019.

Wittmann, A., Kenkmann, T., Schmitt, R., Stöffler, D., 2006. Shock-metamorphosed zircon in terrestrial impact craters. Meteorit. Planet. Sci. 41 (3), 433–454. https://doi.org/10.1111/j.1945-5100.2006.tb00472.x.

Yang, B., et al., 2022. Tectonic controls on sedimentary provenance and basin geography of the Mesoproterozoic Wilton package, McArthur Basin, northern Australia. Geol. Mag. 159 (2), 179–198. https://doi.org/10.1017/S0016756820001223.